

# The Hamburg/ESO R-process Enhanced Star survey (HERES) <sup>★</sup>

## XI. The highly *r*-process-enhanced star CS 29497-004

V. Hill<sup>1</sup>, N. Christlieb<sup>2</sup>, T.C. Beers<sup>3</sup>, P.S. Barklem<sup>4</sup>, K.-L. Kratz<sup>5,6</sup>, and B. Nordström<sup>7,8</sup> B. Pfeiffer<sup>6</sup> K. Farouqi<sup>5,6</sup>

<sup>1</sup> Laboratoire Lagrange, Université de Nice Sophia-Antipolis, Observatoire de la Côte d’Azur, CNRS, Bd de l’Observatoire, CS 34229, 06304 Nice cedex 4, France; e-mail: [vanessa.hill@oca.eu](mailto:vanessa.hill@oca.eu)

<sup>2</sup> Zentrum für Astronomie der Universität Heidelberg, Landessternwarte, Königstuhl 12, 69117 Heidelberg, Germany; e-mail: [N.Christlieb@lsu.uni-heidelberg.de](mailto:N.Christlieb@lsu.uni-heidelberg.de)

<sup>3</sup> Department of Physics and JINA Center for the Evolution of the Elements, University of Notre Dame, Notre Dame, IN 46556, USA; e-mail: [tbeers@nd.edu](mailto:tbeers@nd.edu)

<sup>4</sup> Theoretical Astrophysics, Department of Physics and Astronomy, Uppsala University, Box 516, SE-751 20 Uppsala, Sweden; e-mail: [Paul.Barklem@physics.uu.se](mailto:Paul.Barklem@physics.uu.se)

<sup>5</sup> Max-Planck-Institut für Chemie (Otto-Hahn-Institut), D-55128 Mainz;

<sup>6</sup> Fachbereich Chemie, Pharmazie & Geowissenschaften, Universität Mainz, D-55128 Mainz; e-mail: [klk@uni-mainz.de](mailto:klk@uni-mainz.de), [Dr.Bernd-Pfeiffer@t-online.de](mailto:Dr.Bernd-Pfeiffer@t-online.de), [farouqi@live.de](mailto:farouqi@live.de)

<sup>7</sup> Dark Cosmology Centre, The Niels Bohr Institute, Copenhagen University, Juliane Maries Vej 30, DK-2100, Copenhagen, Denmark; e-mail: [birgitta@nbi.ku.dk](mailto:birgitta@nbi.ku.dk)

<sup>8</sup> Stellar Astrophysics Centre, Department of Physics and Astronomy, Aarhus University, Ny Munkegade 120, DK-8000, Aarhus C, Denmark

Received / Accepted

### ABSTRACT

We report an abundance analysis for the highly *r*-process-enhanced (*r*-II) star CS 29497-004, a very metal-poor giant with  $T_{\text{eff}} = 5013$  K and  $[\text{Fe}/\text{H}] = -2.85$ , whose nature was initially discovered in the course of the HERES project. Our analysis is based on high signal-to-noise, high-resolution ( $R \sim 75000$ ) VLT/UVES spectra and MARCS model atmospheres under the assumption of local thermodynamic equilibrium, and obtains abundance measurements for a total of 46 elements, 31 of which are neutron-capture elements. As is the case for the other  $\sim 25$  *r*-II stars currently known, the heavy-element abundance pattern of CS 29497-004 well-matches a scaled Solar System second peak *r*-process-element abundance pattern. We confirm our previous detection of Th, and demonstrate that this star does not exhibit an “actinide boost”. Uranium is also detected ( $\log \epsilon(\text{U}) = -2.20 \pm 0.30$ ), albeit with a large measurement error that hampers its use as a precision cosmo-chronometer. Combining the various elemental chronometer pairs that are available for this star, we derive a mean age of  $12.2 \pm 3.7$  Gyr using the theoretical production ratios from waiting-point approximation models (Kratz et al. 2007). We further explore the high-entropy wind model (Farouqi et al. 2010) production ratios arising from different neutron richness of the ejecta ( $Y_e$ ), and derive an age of  $13.7 \pm 4.4$  Gyr for a best-fitting  $Y_e = 0.447$ . The U/Th nuclei-chronometer is confirmed to be the most resilient to theoretical production ratios and yields an age of  $16.5 \pm 6.6$  Gyr. Lead (Pb) is also tentatively detected in CS 29497-004, at a level compatible with a scaled Solar *r*-process, or with the theoretical expectations for a pure *r*-process in this star.

**Key words.** stars: metal-poor – stars: *r*-process enhanced – cosmo-chronometry

## 1. Introduction

Even though the physics of the rapid neutron-capture process (*r*-process) has been explored since the seminal works of Burbidge et al. (1957) and Cameron (1957), the astrophysical site(s) and stellar progenitor(s) that could give rise to the extreme conditions needed for its onset remain elusive. The discovery of the first highly *r*-process-element enhanced metal-poor star, CS 22892-052 (Snedén et al. 1994), and the remarkable agreement of its *r*-process-element abundance pattern with the (inferred) Solar System pattern, prompted vigorous exploration of models in which individual core-collapse supernovae are possible sites of the astrophysical *r*-process (see Sneden et al. 2008 for a review). Subsequent searches for such stars, and their de-

tailed spectroscopic follow-up, have revealed that the scaled-Solar heavy-element abundance pattern for very ([VMP:  $[\text{Fe}/\text{H}] < -2.0$  and extremely (EMP:  $[\text{Fe}/\text{H}] < -3.0$ ) metal-poor stars with  $[\text{Eu}/\text{Fe}] > +1.0$  and  $[\text{Ba}/\text{Eu}] < 0.0$  (*r*-II stars: Beers & Christlieb 2005) is extremely robust, and provides what has come to be known as the “universality constraint” on the origin of the *r*-process. Recent theoretical attention has focused on the possibility that merging neutron star (and/or neutron star / black hole) binaries may play a central role in the early production of the *r*-process elements that satisfies the universality constraint (e.g., Ishimaru et al. 2015, and references therein), in particular if they took place in astrophysical environments in which star formation and mixing (dilution) was inefficient. This latter suggestion has been given recent observational support from the discovery of a substantial population of *r*-II stars in the ultra-faint dwarf galaxy Reticulum II (Ji et al. 2016; Roederer et al. 2016), a galaxy which may be similar to the low-mass mini-halos that

Send offprint requests to: V. Hill, e-mail: [vanessa.hill@oca.eu](mailto:vanessa.hill@oca.eu)

<sup>★</sup> Based on observations collected at the European Southern Observatory, Paranal, Chile (Proposal Number 170.D-0010).

contributed to the early chemical enrichment of the halo of the Milky Way.

Besides probing specific alternative progenitors and environments by studies of their observed *r*-process abundance patterns, measurements of the abundances of long-lived radioactive isotopes for *r*-II stars, such as thorium ( $^{232}\text{Th}$ ; half-life  $\sim 14$  Gyr) and uranium ( $^{238}\text{U}$ ; half-life  $\sim 4.5$  Gyr), can also place constraints on the age of the Universe (e.g., Cayrel et al. 2001; Hill et al. 2002). It must be recognized, however, that *r*-II stars are exceedingly rare – comprising no more than 3-5% of *all* VMP and EMP stars. Only two *r*-II stars with unambiguously detected U have been reported in the literature, CS 31082-001 (Hill et al. 2002) and HE 1523-0901 (Frebel et al. 2007).

While the first few *r*-II stars were identified from high-resolution spectroscopic follow-up of VMP and EMP stars selected from the HK survey (Beers et al. 1985, 1992), the Hamburg/ESO R-process Enhanced Star (HERES) survey was the first dedicated effort to substantially increase the numbers of known *r*-II (and *r*-I,  $+0.3 \leq [\text{Eu}/\text{Fe}] \leq +1.0$  and  $[\text{Ba}/\text{Eu}] < 0.0$ ; Beers & Christlieb 2005) stars in the halo of the Milky Way. Its motivations have been described in previous papers of this series (Christlieb et al. 2004, hereafter Paper I; Barklem et al. 2005, hereafter Paper II). In Paper I, we also reported on the discovery of the highly *r*-II star CS 29497-004, and the detection of the Th II line at  $\lambda = 4019.129 \text{ \AA}$  in its HERES “snapshot” spectrum. Herein, we demonstrate that it is now the third metal-poor star known with clearly detected uranium, based on a detailed abundance analysis of high-quality VLT/UVES spectra using MARCS model atmospheres.

For the convenience of the reader, we have summarized the coordinates and photometry of CS 29497-004 in Table 1.

This paper is outlined as follows. The observations and data processing are described in Sect. 2, the determination of the stellar parameters in Sect. 3, and the abundance analysis in Sect. 4. The results are summarized in Sect. 5 and discussed in Sect. 6.

**Table 1.** Coordinates and photometry of CS 29497-004. References: 1 – Paper I; 2 – Beers et al. (2007); 3 – Skrutskie et al. (2006).

Parameter	Value	Ref.
R.A. (2000.0)	00 : 28 : 06.9	1
DEC (2000.0)	−26 : 03 : 04	1
<i>V</i> [mag]	$14.034 \pm 0.005$	2
<i>B</i> − <i>V</i> [mag]	$0.705 \pm 0.010$	2
<i>V</i> − <i>R</i> [mag]	$0.451 \pm 0.006$	2
<i>V</i> − <i>I</i> [mag]	$0.918 \pm 0.007$	2
<i>J</i> [mag]	$12.491 \pm 0.021$	2,3
<i>H</i> [mag]	$12.038 \pm 0.024$	2,3
<i>K</i> [mag]	$11.965 \pm 0.025$	2,3

## 2. Observations, data reduction, and radial-velocity variation

High-resolution spectra of CS 29497-004 were obtained with UVES at VLT-UT2 during October–December 2002 and July–August 2003. A total of 22 exposures were obtained with the BLUE346 setting, and 6 with the BLUE437 setting. In both cases Image Slicer #2 was used, yielding a nominal resolving power of  $R = \lambda/\Delta\lambda = 75,000$ . The total useful wavelength range covered by these two settings is 3050–4980 Å in the rest frame of the star. The observations are summarized in Table 2.

**Table 2.** UVES observations of CS 29497-004.  $\lambda$  refers to the combined useful wavelength range (in the rest frame of the star) of all *N* individual exposures, and *t* is the total integration time.

Setting	$\lambda$ [Å]	<i>N</i>	<i>t</i> [h]
BLUE346	3050-3865	22	21.2
BLUE437	3760-4980	6	4.9

The individual pipeline-reduced spectra were first corrected for geocentric radial-velocity shifts, determined by measuring the positions of  $\sim 10$  clean absorption lines throughout the covered spectral range. Then, the spectra at each setting were co-added using an iterative procedure in which pixels in the individual spectra affected by cosmic ray hits not fully removed during the data reduction, or by CCD defects or other artifacts, were identified. These pixels were flagged and ignored in the final iteration of the co-addition procedure. The co-addition takes into account the *S/N* of the individual spectra (the noise estimate being provided by the UVES pipeline), by computing for each final spectral bin a weighted average of the corresponding bins in the individual spectra.

The resulting co-added spectrum of the BLUE346 setting has a peak *S/N* of  $\sim 150$  per 0.0125 Å pixel in the reddest part of the spectrum, roughly linearly decreasing to *S/N* = 50 at 3300 Å and *S/N* = 10 at 3100 Å. The co-added BLUE437 spectrum has a maximum *S/N* per 0.0152 Å pixel of 120 at 4980 Å, decreasing to  $\sim 60$  at 3760 Å.

In addition, all 28 spectra were co-added in the wavelength range covered by both settings, 3760–3865 Å. The *S/N* did not increase significantly with respect to the 22 co-added BLUE346 spectra, but the additional co-added spectrum has been used for verifying the detection of critical lines such as the U II 3859.57 Å line.

Together with the UVES “snapshot” spectrum taken on 1 November 2001 (see Paper I), the UVES spectra cover a period of about 3 years. During this period of time, no significant radial-velocity variations of CS 29497-004 were detected (see Fig. 1). Hansen et al. (2015) reported on 12 independent high-resolution observations of this star, extending over a temporal window of seven years, and obtained a mean velocity of  $105.0 \pm 0.37$  km/s, which agrees well with our own measurements. When combined with our present measurements and those from Paper I, the temporal window over which this star has not exhibited significant radial-velocity variations expands to  $\sim 13$  years. These data have been examined in detail, and no suitable orbit could be identified (T.T. Hansen, private communication). It thus appears that CS 29497-004 is a single star, consistent with the great majority of *r*-II (and *r*-I) stars in the Hansen et al. (2015) study. These authors report that the binary fraction of *r*-process-element enhanced stars is  $18 \pm 11\%$ <sup>1</sup>, commensurate with that found for other “normal” halo giants.

## 3. Stellar parameters

The stellar parameters of CS 29497-004 adopted throughout this paper are reported in Table 3; they were obtained in the following manner. The effective temperature,  $T_{\text{eff}}$ , that was derived in Paper II, based on a combination of *BVRI* and *JHK* broadband colours and the colour-temperature calibrations of Alonso et al.

<sup>1</sup> Note that the published error bar on this fraction was incorrectly reported as 6%.

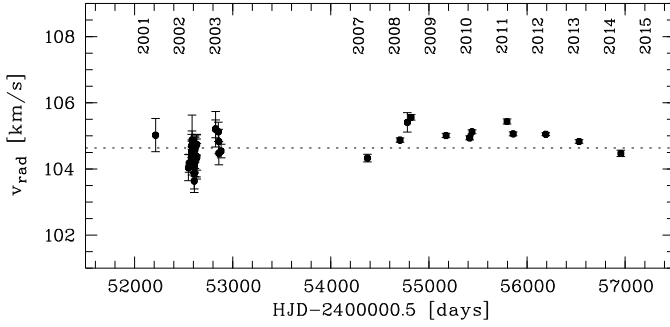


**Fig. 1.** Barycentric radial velocities of CS 29497-004 from the present paper (observations in 2002-2003), those from Paper I (observations in 2001), and from Hansen et al. (2015) (observations in 2007 to 2014). See Table A.1 for a complete list of these data. No significant radial velocity variations were detected on a timescale of  $\sim 13$  years.

(1999), was verified to successfully fulfill the excitation equilibrium for a sample of 77 Fe I lines, and subsequently adopted. Surface gravity,  $\log g$ , was deduced from the ionisation equilibrium of Fe I and Fe II lines. The microturbulence velocity,  $v_{\text{micr}}$ , was deduced by requiring that Fe I lines of all strengths produced the same Fe abundance. Fig. 2 illustrates the adequacy of the stellar parameters to reproduce excitation and ionisation balance as well as a flat behaviour of the abundance with increasing line strength.

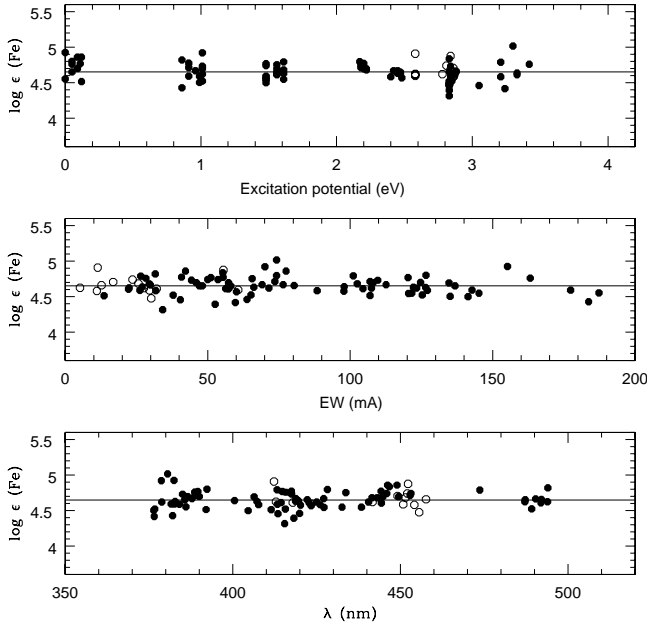


**Fig. 2.** Iron abundances (Fe I filled circles, Fe II open circles) as a function of excitation potential, equivalent width, and line wavelengths, showing the adequacy of the stellar parameters to reproduce excitation and ionisation balance as well as a flat behaviour of the abundance with increasing line strength.

**Table 3.** Stellar parameters of CS 29497-004.

	Paper I	Paper II	This work
$T_{\text{eff}}$ [K]	$5090 \pm 100$	$5013 \pm 100$	$5013 \pm 100$
$\log g$ (cgs)	$2.4 \pm 0.4$	$2.23 \pm 0.24$	$2.05 \pm 0.1$
[Fe/H]	$-2.64 \pm 0.12$	$-2.81 \pm 0.13$	$-2.85 \pm 0.11$
$v_{\text{micr}}$ [km/s]	$1.6 \pm 0.2$	$1.62 \pm 0.13$	$1.60 \pm 0.1$

## 4. Abundance analysis

### 4.1. Model atmospheres

The model atmospheres used in this analysis are the same as those used in the analysis of the  $r$ -II star CS 31082-001 (Cayrel et al. 2001; Hill et al. 2002) and the VMP/EMP giants in the First Stars project (Cayrel et al. 2004). The models are interpolated in a grid of OSMARCS models computed between 2000 and 2002 by B. Plez, using the latest version of the MARCS code. The MARCS code was originally developed by Gustafsson et al. (1975), and updated and improved over the years by Plez (1992), Edvardsson et al. (1993), Asplund et al. (1997), and Gustafsson et al. (2008).

The abundance measurements themselves were carried out using the suite of programs *Turbospectrum* (Alvarez & Plez 1998), either through an equivalent-width analysis, or direct comparison (and  $\chi^2$  minimisation) between the observed and synthetic spectra. The abundances for elements from Mg through Zn were computed using equivalent widths, while the abundances of C, N, O, and of most of the neutron-capture elements, are measured by comparing directly the observed spectrum with synthetic spectra.

### 4.2. Line data

The linelist adopted to determine abundances in this paper is the same as the one used in Hill et al. (2002) and Cayrel et al. (2004), with the exception of a number of neutron-capture elements for which improved atomic data has appeared in recent years, thanks to the efforts of atomic physicists (e.g., Lawler et al. 2001a,c, 2004, 2006, 2007; Nilsson et al. 2002a,b). The neutron-capture element linelist is given in the Appendix (Table B.1), together with the references for transition probabilities and hyperfine structure coefficients, where appropriate.

The atomic linelist used for the spectrum synthesis was assembled using the VALD database (Kupka et al. 1999, 2000), and oscillator strength and/or hyperfine structures were updated for specific lines. The same molecular linelists as in Hill et al. (2002), Spite et al. (2005), and Spite et al. (2006) were included in the syntheses for  $^{12}\text{CH}$ ,  $^{13}\text{CH}$ ,  $^{12}\text{C}^{14}\text{N}$ ,  $^{13}\text{C}^{14}\text{N}$ ,  $^{14}\text{NH}$ ,  $^{15}\text{NH}$ , and  $^{16}\text{OH}$ .

### 4.3. Equivalent-width measurements

Equivalent-width measurements were performed independently by V.H. and N.C.; Fig. 3 shows a comparison of these two sets of measurements. They agree very well for lines weaker than about 100 mÅ. Due to the fact that different relative weights of the line core and wings are implicitly assigned by the fitting procedures used, the equivalent widths of strong lines measured by N.C. are systematically higher than those measured by V.H. In any case, for *both* procedures the equivalent widths of strong lines may be underestimated, because Gaussian profiles were used. Ideally, Voigt profiles should be used for the fits to strong lines, since they exhibit damping profiles.

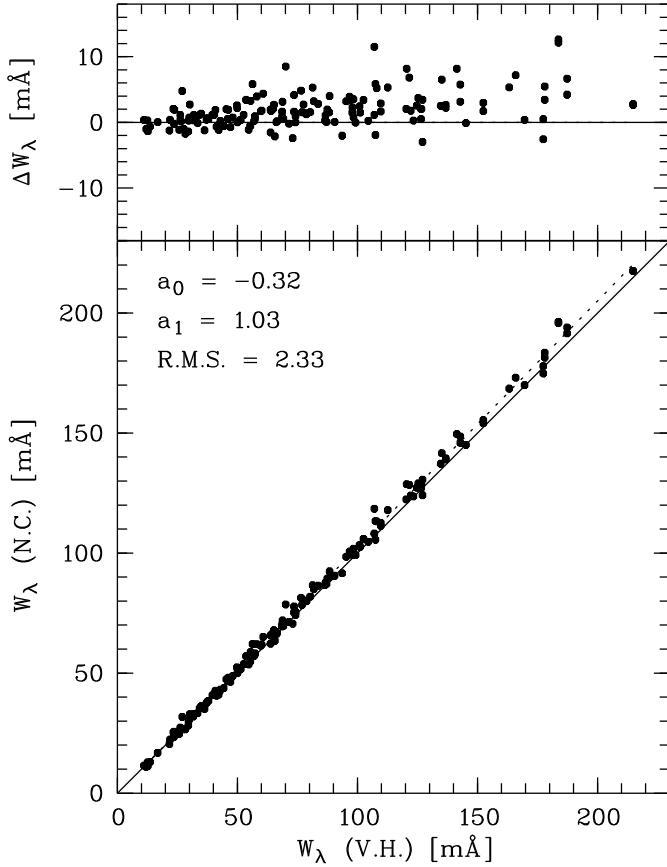


**Fig. 3.** Equivalent widths for 156 lines of 12 elements, up to the Fe peak. The initials on each axis indicate the authors who (independently) performed these measurements. The solid line is the one-to-one line, while the dashed line indicates a linear fit to the data.

In order to be consistent with the analysis of CS 31082-001 (Cayrel et al. 2001; Hill et al. 2002), we adopted the measurements of V.H. for the equivalent-width analysis.

#### 4.4. C, N, and O abundances

The elements carbon, nitrogen and oxygen are detected via molecular bands of CH, NH, and OH. Molecular equilibrium is solved including all relevant molecules for the atmosphere of cool stars, including CO which plays a major role in the C,N,O molecular equilibrium.

The carbon abundance is derived primarily from CH lines in the region 4290-4310 Å (the CH A-X 0-0 bandhead, often referred to as the *G*-band), which is almost free from intervening atomic lines. We derive an abundance  $\log \epsilon(\text{C}) = 5.94 \pm 0.5$  (see Fig. 4). With this same abundance, a good fit is obtained in the more crowded regions around 3900 Å and 3150 Å, where the B-X and C-X bandheads occur. The  $^{12}\text{C}/^{13}\text{C}$  ratio is constrained to  $^{12}\text{C}/^{13}\text{C} = 20^{+12}_{-7}$  from ten  $^{13}\text{CH}$  A-X lines in the region 4230-4250 Å. This  $^{12}\text{C}/^{13}\text{C}$  ratio is comparable with that observed in other metal-poor red giants that have not yet experienced extra-mixing events arising at the red giant branch (RGB) bump (Spite et al. 2006), confirming that CS 29497-004 sits on the lower RGB (below the RGB bump).

The nitrogen abundance is derived from the violet NH band  $\text{A}^3\Pi_i - \text{X}^3\Sigma^-$  at 3360 Å, and yields  $\log \epsilon(\text{N}) = 5.35 \pm 0.1$  (see Fig. 5). The CN molecule (3875-3900 Å B-X 0-0 bandhead) is

not detectable in CS 29497-004, in agreement with the synthetic spectrum computed using the C and N abundances derived from CH and NH, respectively.

The OH lines in the UV portion of the spectrum permit measurements of the oxygen abundance, based on twelve lines around between 3120 Å and 3180 Å. The resulting oxygen abundance is  $\log \epsilon(\text{O}) = 6.60 \pm 0.1$ . This oxygen abundance ( $\log \epsilon(\text{O}) = 6.60$ ) was used to derive the C and N abundances above, and is used throughout the paper for all other synthesis, unless specified otherwise. However, we find that there is a dependence of the abundance on the OH line strength, the weaker lines giving lower oxygen abundances. This illustrates that in EMP stars, molecules (not only OH, but also CH, NH, and CN) that form high up in the stellar atmosphere are sensitive to 3D effects, and probably also to NLTE effects, as emphasized by Asplund (2005), and more specifically for giants by Collet et al. (2007). In the latter work, a dependence on the 1D to 3D correction on the excitation potential (E.P.) of the OH lines is expected, and this is also confirmed with a different 3D code by Dobrovolskas et al. (2013). This could (at least partly) explain the variations found here between the weak and strong O lines. All lines measured here around 3120-3180 Å have E.P. in the range 0.1 to 0.8 eV, while the weak OH lines found around 3300 Å have E.P. around 1.5 eV. For CS 29497-004, a significantly lower O abundance of  $\log \epsilon(\text{O}) = 6.30 \pm 0.15$  is found when evaluated from these particular weak lines (see Fig. 6).

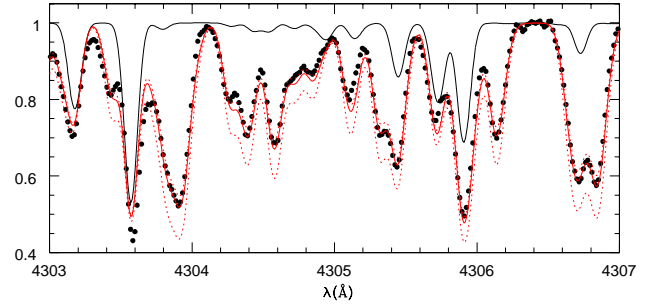


**Fig. 4.** Observed (dots) and synthetic spectra (lines) around the CH A-X bandhead (*G*-band) at 4300 Å, where the solid and dashed red lines are computed with  $\log \epsilon(\text{C}) = 5.89, 5.94$ , and  $6.09$ , and the solid black line is a synthetic spectrum without CH molecular lines.

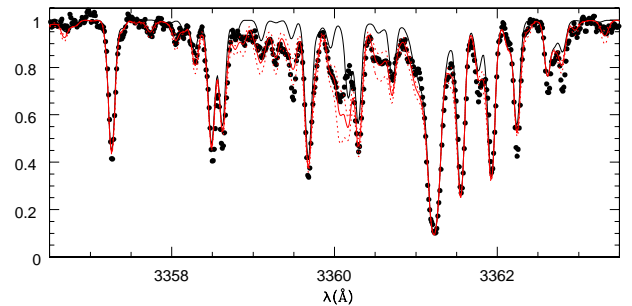


**Fig. 5.** Observed (dots) and synthetic spectra (lines) around the NH bandhead at 3360 Å, where the solid and dashed red lines are computed with  $\log \epsilon(\text{N}) = 5.15, 5.35$ , and  $5.55$ , and the solid black line is a synthetic spectrum without NH molecular lines.

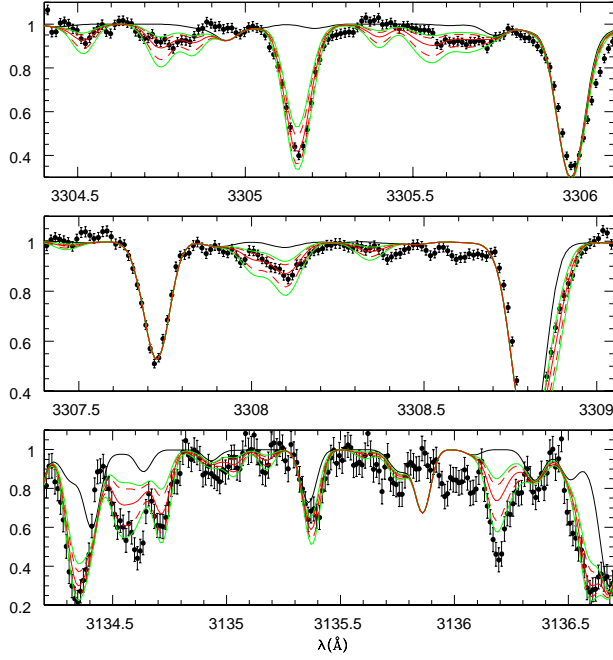


**Fig. 6.** Observed (dots) and synthetic spectra (lines) around various OH lines, where the solid and dashed red and green lines are computed with  $\log \epsilon(\text{O}) = 6.00, 6.10, 6.30, 6.50$ , and  $6.60$ , and the solid black line is a synthetic spectrum without OH molecular lines.

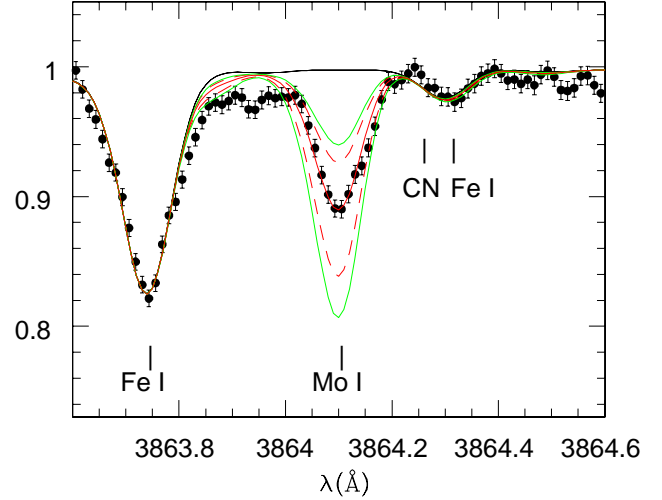


**Fig. 7.** Observed (dots with error bars) and synthetic spectra (lines) around the Mo line at  $3864.10 \text{ Å}$  for abundances of  $\log \epsilon(\text{Mo}) = -0.15, -0.05, 0.05, 0.15, 0.25, 0.35, 0.45$ , and no Mo.

#### 4.5. Neutron-capture elements

The abundances for individual lines of the neutron-capture elements are given in Table B.1, together with the method that was used to derive them. When the lines were sufficiently isolated, and no hyperfine structure is present, the abundances were deduced from equivalent widths, while line-profile fitting with spectrum synthesis was performed in all other cases, including all the weakest lines.

Below, we comment on the detection of special lines, element by element.

##### 4.5.1. Light *r*-process elements: $39 < Z \leq 48$

**Molybdenum:** This species has only one weak line detectable from the ground, at  $3864.10 \text{ Å}$ . In the carbon-enhanced *r*-II star CS 22892-052, Sneden et al. (2003) remark that, in addition to being very weak, the Mo line sits quite close to a CN line, which could account for at least a part of the absorption at the Mo wavelength. Fortunately, CS 29497-004 has extremely low C and N content, and no CN absorption is visible in the spectrum. The Mo line therefore appears clean in our spectrum, and is very clearly detected, as illustrated in Fig. 7.

We searched for cadmium (Cd at  $3261.0 \text{ Å}$ ) and tin (Sn at  $3262.3$  and  $3801.0 \text{ Å}$ ), but these transitions were too weak and too blended to enable detection.

##### 4.5.2. Second *r*-process peak elements: $56 < Z \leq 72$

**Lutetium:** The lutetium abundance in CS 29497-004 was measured with the Lu II  $3397 \text{ Å}$  line (see Fig. 8), and further checked using the very weak Lu II features at  $3472.45$  and  $3554.39 \text{ Å}$ . Despite the fact that the  $3397 \text{ Å}$  line is in the wing of an Fe I

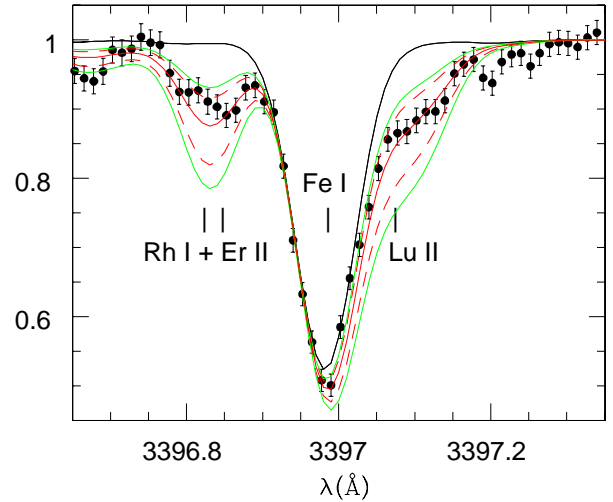


**Fig. 8.** Observed (dots with error bars) and synthetic spectra (lines) around the Lu line at  $3397 \text{ Å}$  for Lu abundances of  $\log \epsilon(\text{Lu}) = -1.02, -0.92, -0.72, -0.52$ , and  $-0.42$  as red and green lines, and no Lu (black line). Despite the fact that this line is in the wing of an Fe I line, the abundance of Lu is well-constrained.

##### 4.5.3. Third *r*-process peak elements and the actinides: $72 < Z \leq 92$

**Platinum:** From the ground, the only metal-poor star in which platinum has been detected so far is the *r*-II star CS 22892-052 (Sneden et al. 2003), from two lines at  $3301.9$  and  $3315.0 \text{ Å}$ . Pt detections were obtained for a handful of other metal-poor stars from stronger lines in the near-UV around  $2650$  and  $2900 \text{ Å}$  with

HST/STIS (e.g., Westin et al. 2000; Cowan et al. 2002; Barbuy et al. 2011).

The 3315.0 Å Pt I line is not detected in our spectrum (the continuum in this region is not sufficiently clean to permit detection of this line, which has an equivalent width of only a few mÅ). The 3301.87 Å feature is stronger and clearly visible, but an OH line is predicted to fall right on top of it (at 3301.85 Å), accounting for ~40% of the total absorption at the Pt wavelength. An oxygen abundance of  $\log \epsilon(\text{O}) = 6.30 \pm 0.15$  has been used to model OH lines in the wavelength region around the Pt line at 3301 Å (see discussion in section 4.4). The uncertainty in the OH feature translates into a 0.2 dex uncertainty in the Pt abundance for CS 29497-004 (see Fig. 9). We further checked that in the *r*-process-poor star HD 122563 ( $[\text{Fe}/\text{H}] = -2.71$ ,  $T_{\text{eff}} = 4625$  K,  $\log g = 1.4$ ; Cayrel et al. 2004), where no Pt is visible, the relative strengths of the OH lines at 3301.85 Å (blending the Pt line), 3305.7 Å, and 3308.3 Å, (employed to set the O abundance) were successfully reproduced by a synthetic spectrum using the same OH linelist. This strengthens our measurement of the Pt abundance for CS 29497-004. We further note that, for CS 22892-052, where Pt is detected both at 3301.87 Å and through the cleaner and stronger UV line at 2929.82 Å (Snedden et al. 2003), both abundances agree well (within 0.15 dex).

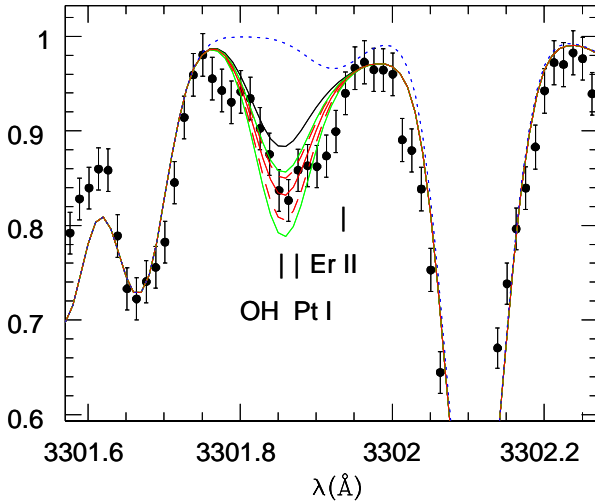


**Fig. 9.** Observed (dots with error bars) and synthetic spectra (lines) around the Pt line at 3301.87 Å for abundances of  $\log \epsilon(\text{Pt}) = -0.3, -0.2, 0.0, +0.2$ , and  $+0.3$  (green and red full and dashed curves). In addition, a synthesis with no Pt (black full line) shows the prominent OH blend, while the upper dotted blue curve shows a synthesis without Pt and OH, revealing a faint Er II line in the red wing of the feature, which has no impact on the Pt abundance determination.

**Lead:** Lead is on the edge of detection for CS 29497-004 with our current spectra. The 3665 Å line is not detected, while the 4057.8 Å feature is exceedingly weak, and in the vicinity of a  $^{12}\text{CH}$  feature (from the B-X system), only allowing an upper limit on the Pb abundance to be derived. A conservative upper limit of  $\log \epsilon(\text{Pb}) < +0.25$  is derived from  $\chi^2$  minimisation (at a 90% confidence level), independent of the assumed carbon abundance for the nearby  $^{12}\text{CH}$  transition (see Fig. 10). The actual minimum of the  $\chi^2$  is reached for  $\log \epsilon(\text{Pb}) = -0.25$ . Both values are reported in Table 5.

**Thorium:** Owing to the high levels of *r*-process elements in CS 29497-004, the radioactive element Th is measured from a total of six lines, all of which have accurate oscillator strength data from Nilsson et al. (2002b). The abundances from these lines all agree with one another within the errors; four of these six detections are illustrated in Fig. 11. Note in particular that, thanks to the low C content of this star, the commonly employed 4019 Å line is virtually free of the  $^{13}\text{CH}$  contamination from which it suffers in C-enhanced stars.

**Uranium:** The radioactive element U is very difficult to detect, because most of its transitions are weak and blended. The U transition detected for CS 29497-004 (at 3859.57 Å) lies in the wing of a Fe I line at 3860 Å. To date, uranium has only been unambiguously detected in two EMP stars: CS 31082-001 (Cayrel et al. 2001; Hill et al. 2002) and HE 1523-0901 (Frebel et al. 2007). With a temperature of 5013 K, CS 29497-004 is slightly warmer than both of these stars (with  $T_{\text{eff}}$  of 4825 and 4630 K respectively) and lower on the RGB ( $\log g = 2.05$  instead of 1.55 and 1.00, respectively, for the other two stars). This results in the U line being intrinsically weaker (and the wing of the Fe I line being relatively stronger) for CS 29497-004. Nevertheless, we could detect uranium for CS 29497-004 at a level of  $\log \epsilon(\text{U}) = -2.20 \pm 0.3$  (see Fig. 12). We have carefully examined potential sources of uncertainties that most affect the measurement of uranium: photon noise, and continuum placement and Fe I-wing modelling.

- Photon noise: The expected noise in the spectrum was propagated throughout the reduction chain from the raw image to the final co-added spectrum; error bars in Fig. 12 reflect this noise. Since the U-line region is covered by 28 spectra, we also estimated the standard deviation around the weighted average of all spectra for each pixel. This standard deviation is extremely close to the error propagated along the reduction chain, demonstrating that our estimate of the noise is indeed valid. According to these various methods of estimating the noise, total *S/N* ratios of 170 to 200 are measured per 0.012 Å pixel in this region. Of these individual spectra, 22 were taken with the B436 setting and 6 from the B437 setting. We also compared, in the U-line region, the spectra co-added separately for the two settings. The line profiles are indistinguishable within their respective error bars.
- Continuum placement and Fe I wing: The placement of the continuum is of course an important factor in the fit of a line as weak as the U transition. It was determined in regions clean of lines surrounding the region of interest – around 3859.0 Å and 3860.4 – 3860.6 Å. However, the continuum placement, by itself, is not the primary limiting factor that influences measurement of the uranium line. The blue wing of the 3859.9 Å Fe I line, at the temperature of CS 29497-004, is the dominant absorption feature immediately to the red of the U line. With the adopted continuum, we adjusted the line broadening of the Fe I line to ensure that its red wing (which is essentially free of blends) would fit the observed spectrum as closely as possible. The combined uncertainties of this and the continuum placement amount to a  $\sim 0.2$  dex uncertainty on the measured uranium abundance.

## 5. Results

### 5.1. C through Zn

The abundances of all elements from Mg through Zn were measured using equivalent widths, and are reported in Table 4. CS



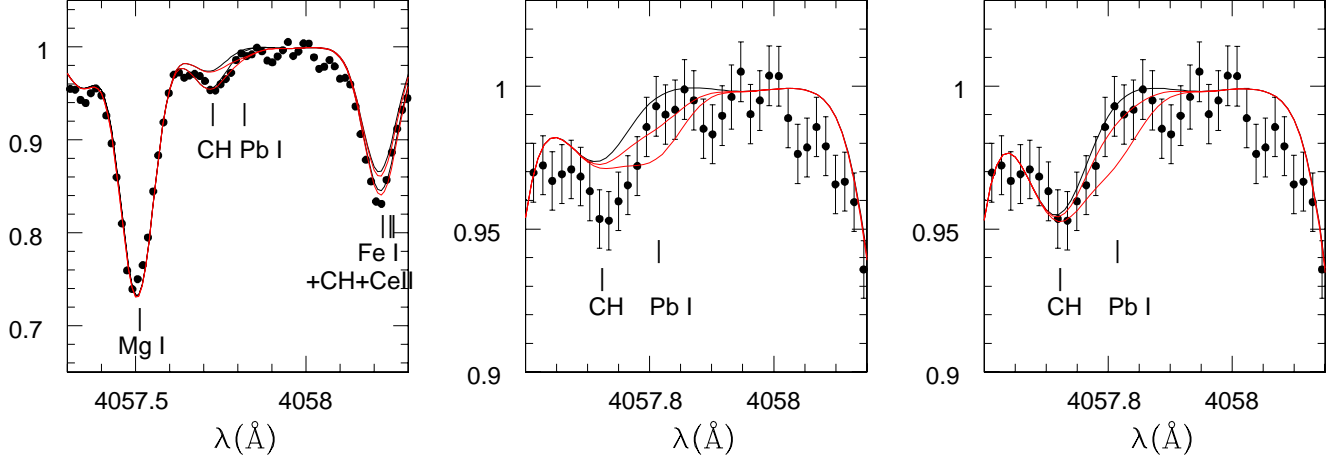


**Fig. 10.** Observed (dots with error bars) and synthetic spectra (lines) around the Pb line at 4057.8 Å. This Pb line lies in the red wing of a weak  $^{12}\text{CH}$  feature (from the B-X system), which proved to be underestimated with the carbon abundance derived from the G-band ( $^{12}\text{CH}$  A-X system), as shown in the middle panel. Two hypotheses for the abundances of carbon have therefore been considered here: (1) The nominal abundance  $\log \epsilon(\text{C}) = 5.94$  (middle panel), and (2) An abundance  $\log \epsilon(\text{C}) = 6.20$ , which best fits the CH 4057.7 Å line (right panel). The left panel shows together the best-fit values for Pb (red curves) and the synthesis with no Pb (black curves) in these two cases. (*middle panel*) Syntheses are shown for  $\log \epsilon(\text{Pb}) = -0.15$  and  $+0.25$  (respectively, the best-fit and a conservative upper limit, shown in red), and no Pb, assuming the nominal C abundance. (*right panel*)  $\log \epsilon(\text{Pb}) = -0.25$  and  $+0.25$  (respectively, the best-fit and a conservative upper limit, shown in red), and no Pb, assuming  $\log \epsilon(\text{C}) = 6.20$ .

29497-004 does not stand out in any particular way compared to other giants of similar low metallicity in the Galactic halo, as probed for example by Cayrel et al. (2004), Barklem et al. (2005), Lai et al. (2008), or Roederer et al. (2014b). It exhibits (in the LTE approximation) the same overabundances of the  $\alpha$ -elements (Mg, Si, Ca, Ti) as well as Co, Zn, and typical underabundances of Al, Cr, and Mn. We caution that these are LTE abundances, and recall that NLTE and/or 3D effects can alter these results (see, e.g., Asplund 2005, for a review). In the case of Al, for example, large NLTE departures are expected: Andrievsky et al. (2008) have shown that NLTE corrections for the lines used in EMP stars are strong, and rely sensitively on the stellar atmospheric parameters. For giants, the hotter and the more metal-poor the star, the stronger the NLTE effects, while the more luminous the giant, the weaker the NLTE corrections. For a giant of  $T_{\text{eff}} = 5000$  K,  $\log g = 2$ ,  $[\text{Fe}/\text{H}] = -3$  (similar to CS 29497-004), the expected NLTE correction for Al is on the order of  $+0.7$  dex, which would bring the aluminum abundance of CS 29497-004 back to a Solar  $[\text{Al}/\text{Fe}]$  ratio.

The abundances of C, N, and O for CS 29497-004 are also reported in Table 4. We emphasise that these abundances are computed in 1D LTE, and could be subject to relatively large revisions once the 3D and NLTE effects are taken into account. As an illustration, the 1D to 3D corrections for a  $T_{\text{eff}} = 5050$  K giant of similar gravity to CS 29497-004 amount to about  $-1.1$  dex for OH,  $-0.7$  dex for CH and  $-0.9$  dex for NH, according to Collet et al. (2007). Under these assumptions, the 3D CNO abundances of CS 29497-004 would be all sub-Solar,  $[\text{C}/\text{Fe}] = -0.3$ ,  $[\text{N}/\text{Fe}] = -0.5$ , and  $[\text{O}/\text{Fe}] = -0.3$ , respectively. Again, the 1D LTE C, N and O abundances found here are in agreement with those of giants in the sample of Spite et al. (2005). More specifically, both the C and N abundances, as well as the isotopic ratio  $^{12}\text{C}/^{13}\text{C}$  of CS 29497-004, are as expected for its luminosity (below the RGB bump), similar to the *unmixed* giants of Spite et al. (2005) and Spite et al. (2006). These stars have all passed the first dredge-up, but have not (yet) experienced strong extra

mixing of internal CNO-cycled material that is triggered by the fading of the molecular-weight barrier at the RGB bump.

In summary, the lighter element abundances from C to Zn in CS 29497-004 are indistinguishable from other EMP giant stars of the same metallicity.

**Table 4.** Abundances of the elements up to the iron peak for CS 29497-004. The Solar C, N, and O abundances were taken from the 1D MARCS analysis of Asplund et al. (2005), while all other Solar abundances are from Grevesse & Sauval (2000).

Z	Species	$\log \epsilon_{\odot}$	$\log \epsilon$	$\sigma$	$N_{\text{lines}}$	$[\text{X}/\text{Fe}]$
6	$^{12}\text{C}/^{13}\text{C}$	80	20	$^{+12}_{-7}$		
6	C (CH)	8.42	5.94	0.05		0.37
7	N (NH)	7.82	5.35	0.10		0.38
8	O (OH)	8.72	6.60	0.10		0.73
12	Mg I	7.58	5.11	0.27	5	0.38
13	Al I	6.47	2.81	0.00	1	-0.81
14	Si I	7.55	5.16	0.11	2	0.46
20	Ca I	6.36	3.81	0.13	5	0.30
21	Sc II	3.17	0.42	0.07	4	0.10
22	Ti I	5.02	2.40	0.03	4	0.23
22	Ti II	5.02	2.45	0.09	22	0.28
24	Cr I	5.67	2.50	0.04	3	-0.32
25	Mn I	5.39	2.31	0.12	5	-0.23
26	Fe I	7.50	4.65	0.12	77	0.00
26	Fe II	7.50	4.66	0.12	13	0.01
27	Co I	4.92	2.45	0.05	4	0.38
28	Ni I	6.25	3.54	0.01	2	0.14
30	Zn I	4.60	2.04	0.00	2	0.29

## 5.2. Neutron-capture elements

The final neutron-capture element abundances for CS 29497-004 are listed in Table 5, and plotted as a function of atomic number in Fig. 14. The table contains, in addition to the mean

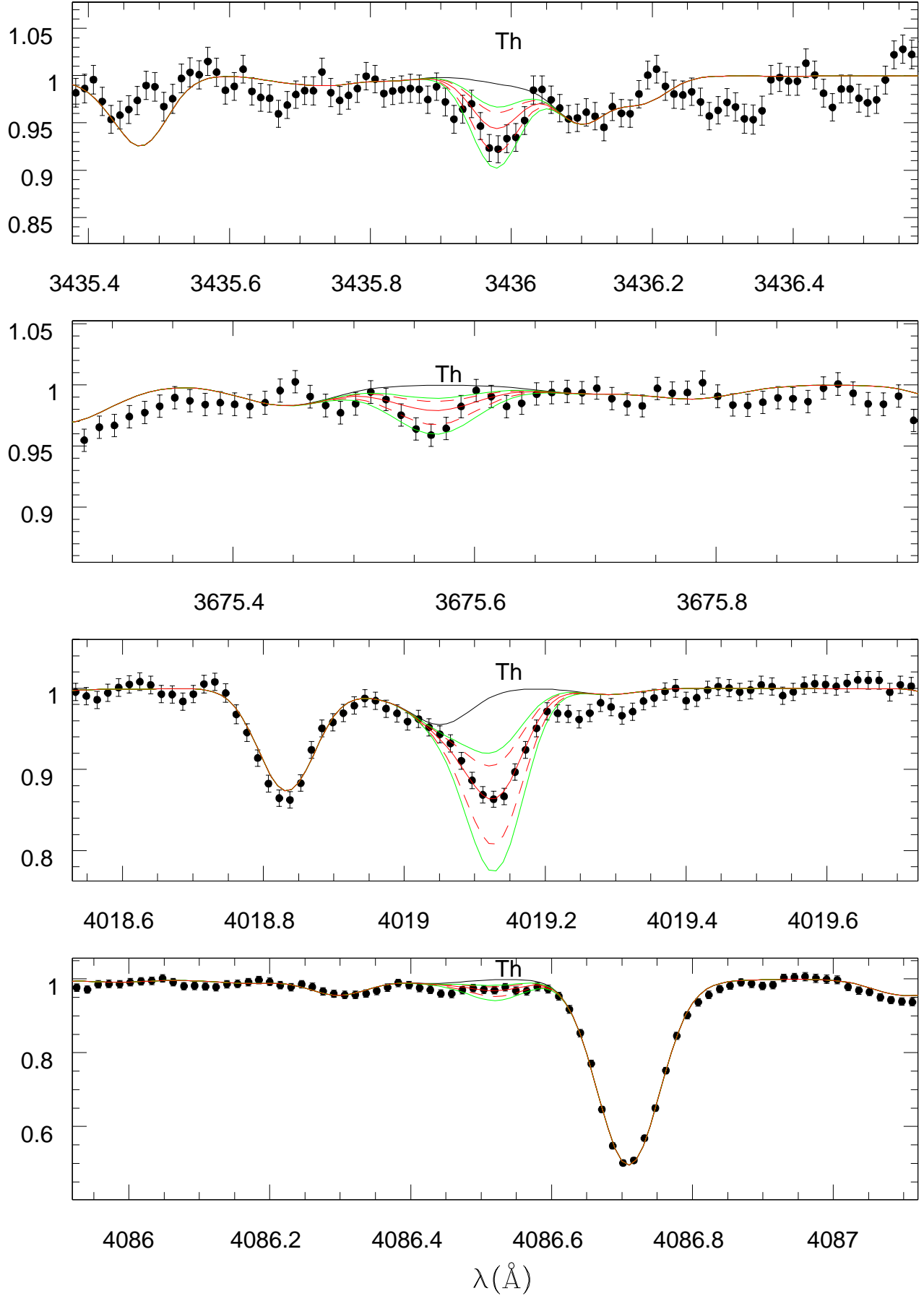


**Fig. 11.** Observed (dots with error bars) and synthetic spectra (lines) around four Th lines for abundances of  $\log \epsilon(\text{Th}) = -1.55, -1.45, -1.25, -1.05, -0.95$ , and no Th.



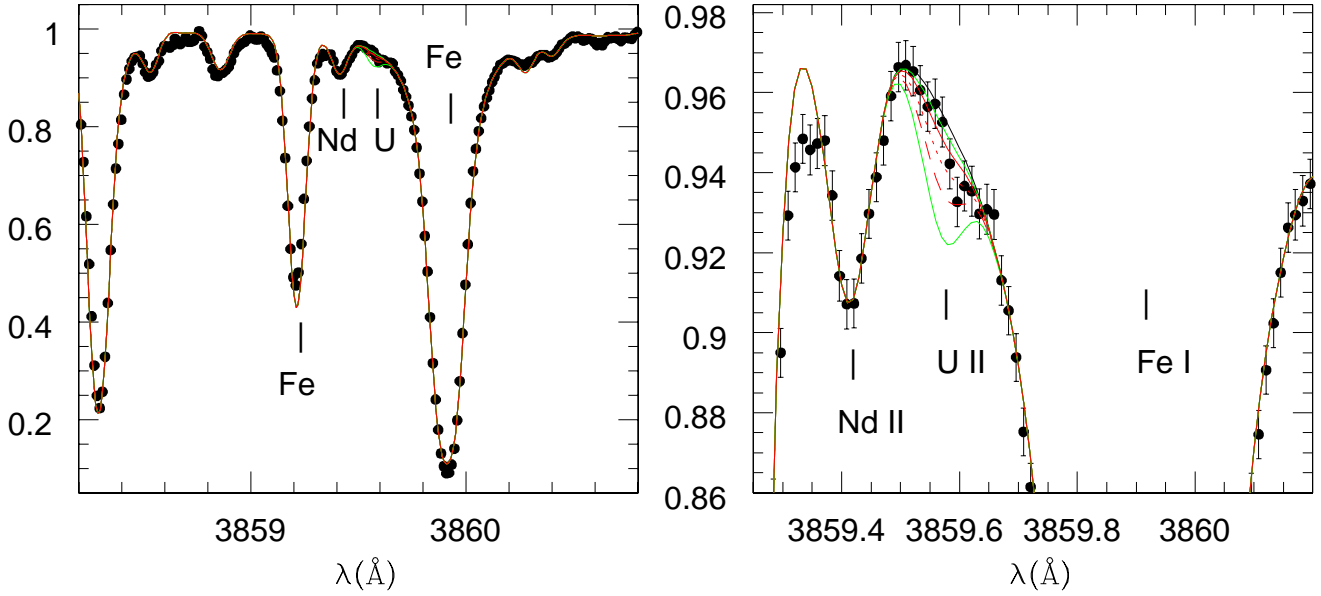


**Fig. 12.** Observed (dots with error bars) and synthetic spectra (lines) around the uranium line at 3859.57 Å for abundances of  $\log \epsilon(\text{U}) = -2.50 - 2.20 - 1.90 - 1.50$ , and no U.

abundance for each element, the dispersion around the mean ( $\sigma$ ), the number of lines used in the analysis ( $N_{\text{lines}}$ ), and the total error on the  $[\text{Th}/\text{X}]$  ratio ( $\sigma_t$ ). This last error estimate takes into account both the total measurement error and the effect of the stellar parameter uncertainties on the  $[\text{Th}/\text{X}]$  ratio ( $\sigma_m$ ), combining both sources in quadrature. The total measurement error itself is computed as the quadratic sum of the errors on element X and Th, estimated as  $\max[\sigma(\text{X})/\sqrt{N(\text{X})}, \sigma_{\text{expected}}(\text{X})]$ , where  $\sigma_{\text{expected}}$  is the propagated individual-line measurement error, and  $\sigma(\text{Th})/\sqrt{N(\text{Th})}$  respectively.

### 5.2.1. CS 29497-004 versus Solar *r*-process abundances

As illustrated in Fig. 13, the abundances of the neutron-capture elements for CS 29497-004 agree well with the Solar System *r*-process distribution, as derived by Arlandini et al. (1999), Simmerer et al. (2004), or Bisterzo et al. (2014), the latter using an updated Solar composition by Lodders et al. (2009) relying mostly on meteoritic abundances for neutron-capture elements. The respective offsets of the CS 29497-004 abundances with respect to these Solar System *r*-process decomposition are:  $\log \epsilon(\text{X}) - \log \epsilon(\text{X}_{\text{r}\odot}) = -1.15 \pm 0.14$  dex,  $\log \epsilon(\text{X}) - \log \epsilon(\text{X}_{\text{r}\odot}) = -1.12 \pm 0.15$  dex, and  $\log \epsilon(\text{X}) - \log \epsilon(\text{X}_{\text{r}\odot}) = -1.10 \pm 0.16$  dex (these offsets were computed for all measured elements with  $56 \leq Z \leq 72$ ). Taken together with the iron abundance of  $[\text{Fe}/\text{H}] = -2.85$  for CS 29497-004, this confirms the very strong *r*-process-element enhancement of this star, by some 1.7 dex, or a factor of 50.

The overall agreement of the observed heavy-element abundances with the Solar *r*-process pattern is best for the second *r*-process peak elements ( $55 < Z < 75$ ). Lutetium, at  $Z = 71$ , is the only element showing a discrepancy  $> 0.25$  dex, which may arise partly from the observational error associated with the detection of this element (see Sect. 4.5.2).

The lighter *r*-process elements ( $37 < Z < 48$ ) are not as well-reproduced by the Solar System decompositions. Although the scaled pattern of Simmerer et al. (2004) is in slightly better

agreement with the observed abundances, the difference among the three Solar System *r*-process decompositions indicates that the *r*-process fraction of these elements suffer from more uncertainties in this atomic mass range, perhaps not surprisingly given that their Solar System total abundance is dominated by the *s*-process contribution. The Bisterzo et al. (2014) work uses the most up-to-date *s*-process prescriptions, so that the decomposition based on this work should be the most reliable of all presented here. In this framework, the first-peak *r*-process elements in CS 29497-004 appear relatively less abundant than the second-peak *r*-process elements, as compared to the Solar System *r*-process decomposition. Since all rII stars share very similar first-peak to second-peak *r*-process elements ratio (ex. Sr/Ba) ratios (see Sec. ), the same conclusion would hold for other rII stars too: the Solar System *r*-process has a higher first-peak to second-peak *r*-process elements than rII stars. Although it cannot be excluded that this excess is simply caused by uncertainties on the Solar System decomposition, this may be related also to the observation that extremely metal-poor stars with milder or no *r*-process enhancements also have higher first-peak to second-peak *r*-process elements ratios than rII stars (see, e.g. Siqueira Mello et al. 2014 and this has been known since McWilliam 1998). Both these facts may be understood if *r*-II stars are polluted by the *main r*-process only, thus hiding the contribution from the *weak r*-process that contributes significantly to the first-peak *r*-process elements in the early Galaxy (see, e.g. Wanajo et al. 2006).

Among elements of the third *r*-process peak, Pt ( $Z = 78$ ) and Pb ( $Z = 82$ ) are most strikingly under-represented by the scaled-Solar *r*-process, whereas Os and Ir are in reasonable agreement. We note however that, according to the update of the Ir partition function proposed by Mashonkina et al. (2010), our Ir abundance could be underestimated by 0.2 dex, which would bring Ir up to the same level as Os, some 0.2 dex above the Solar *r*-process decomposition.

Concerning Pb, there is now a consensus that the *s*-process contribution to Pb computed for the Solar System in the decom-

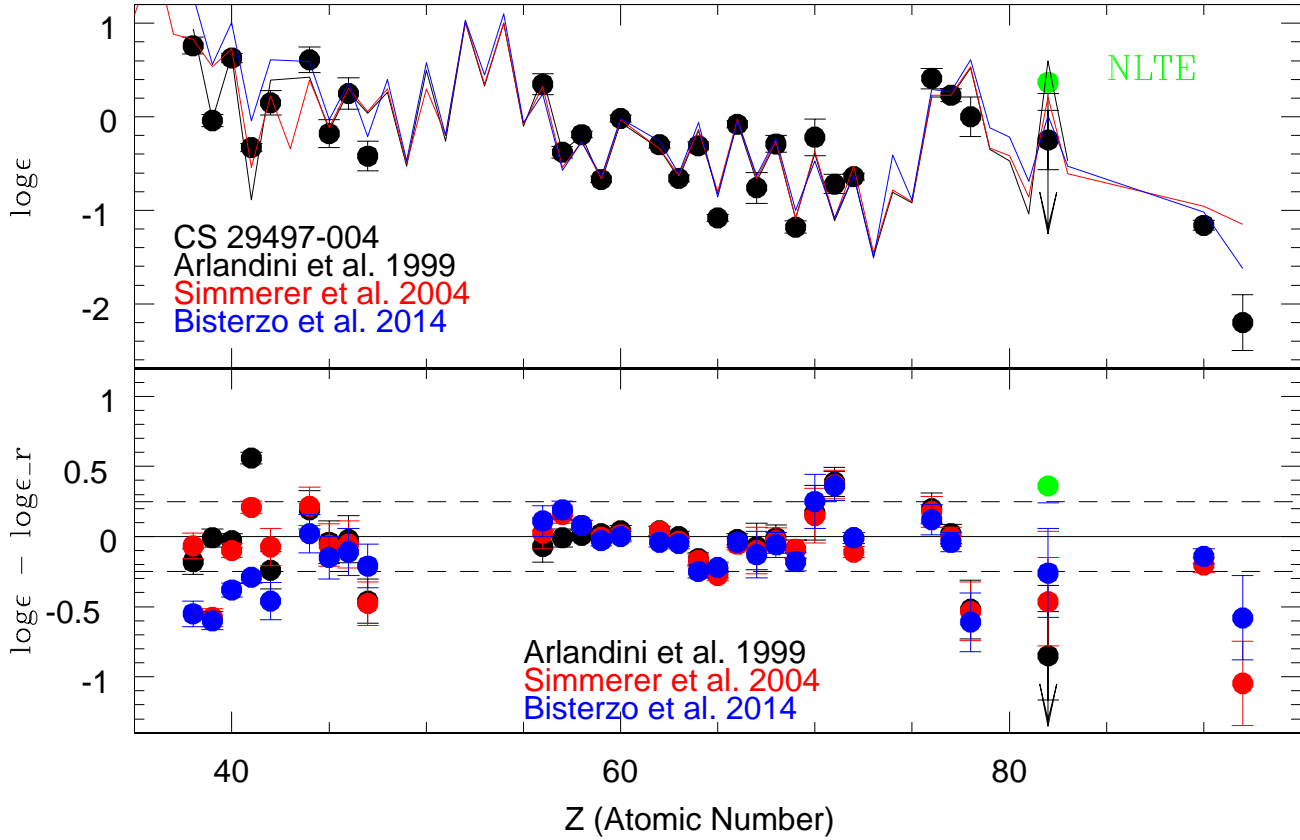


**Fig. 13.** *Upper panel:* Neutron-capture element abundances for CS 29497-004 plotted against atomic number, and compared to the Solar  $r$ -process abundances, following the decompositions of Arlandini et al. (1999) (black line), Simmerer et al. (2004) (red line), and Bisterzo et al. (2014), using the Lodders et al. (2009) Solar composition (blue line). *Lower panel:* Residuals of the abundances for CS 29497-004 to the Solar  $r$ -process decompositions, normalised to the mean  $r$ -process element abundances with  $55 < Z < 73$ . The green point in both panels corresponds to the Pb abundance in CS 29497-004 corrected for NLTE as of Mashonkina et al. (2012).

positions of Arlandini et al. (1999) and Simmerer et al. (2004) were underestimated (see, e.g., Roederer et al. 2009, and references therein). Of central importance, Arlandini et al. (1999) did not take into account the so-called *strong s-process* contribution to Pb in their decomposition (a component now identified as the contribution from metal-poor AGB stars integrated over the history of Galactic chemical evolution, see, e.g., Travaglio et al. 2001, 2004), which would lead to an increase in the total  $s$ -process contribution to Pb from 46% to 83% (Serminato et al. 2009), thereby decreasing the remaining Solar  $r$ -process Pb abundance by about 0.5 dex compared to the original Arlandini et al. (1999) decomposition shown in Fig. 13 (upper panel). In addition, because Pb is dominated by the  $s$ -process in the Solar System, any uncertainty in the total  $s$ -process Pb contribution leads to a substantial variation of the Solar System  $r$ -process component of Pb. This is visible also in the variations among the three Solar System decompositions shown in Fig. 13. The most recent decomposition, Bisterzo et al. (2014), including all the contributions of the  $s$ -process to Pb (reaching 87%), is indeed now in agreement with the low upper limit we report here for CS 29497-004 (see Fig. 13, lower panel).

Thorium and uranium both lie below the Solar System  $r$ -process decomposition, as both of these elements have decayed significantly more in the old star CS 22497-004 than in younger Solar System material.

#### 5.2.2. Abundances in CS 29497-004 compared to other $r$ -II stars with available Th and U measurements

The overall abundance pattern of CS 29497-004 is also very close to that observed in previously discovered  $r$ -II stars with Th and U measurements, the best studied of which are CS 22892-052 (Sneden et al. 1996, 2000, 2003; Sneden et al. 2009), CS 31082-001 (Hill et al. 2002; Sneden et al. 2009; Barbuy et al. 2011; Siqueira Mello et al. 2013), and HE 1523-0901 (Frebel et al. 2007; Sneden et al. 2009). Among the significant differences that are found, we highlight three:

*Uranium and thorium* are lower for CS 29497-004 than for CS 31082-001, which displays an anomaly of the heaviest  $r$ -process nuclei, also known as the *actinide boost* (Hill et al. 2002). In fact, Hayek et al. (2009) suggested that some 30 to 50% of all  $r$ -II stars exhibit this boost. Mashonkina et al. (2014) refined this estimate to 6 of 18 stars (i.e., 33%). CS 29497-004 does not belong to this class, but rather exhibits a ratio of Th to second  $r$ -process peak elements compatible with that of CS 22892-052, which is also commensurate with a standard  $r$ -process and the decay of Th over the age of the Universe.

*Platinum* is significantly lower for CS-29497-004 than for CS 22892-0052. We note that the Pt abundances for these two stars were determined from different lines (see Sec. 4.5.3); this may be the reason for the discrepancy. Additionally, our Pt measurement has a rather large error bar, owing to a blend with an

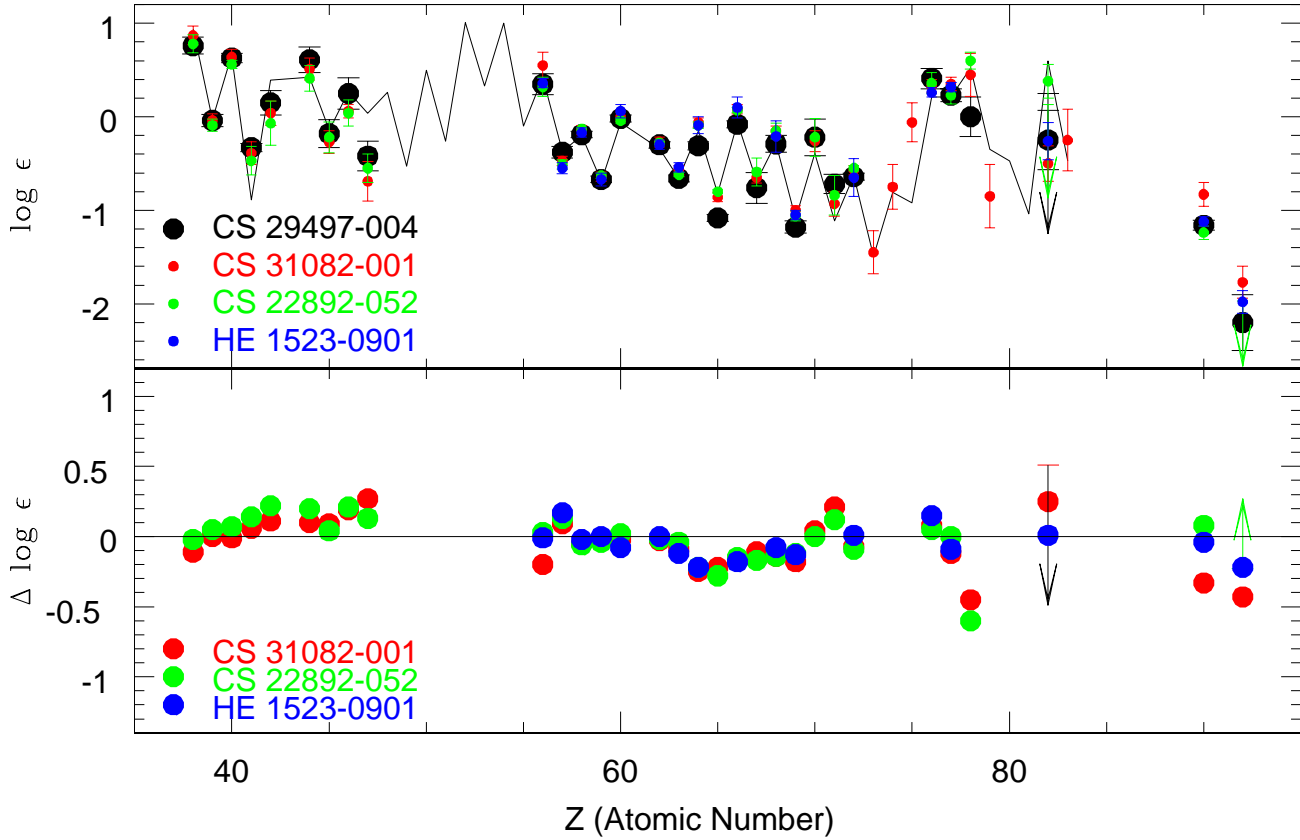


**Fig. 14.** *Upper panel:* Neutron-capture element abundances for CS 29497-004 (black), compared to those in other *r*-II stars (normalised at Ce): CS 31082-001 (red, Hill et al. 2002; Sneden et al. 2009; Barbuy et al. 2011; Siqueira Mello et al. 2013), CS 22892-052 (green, Sneden et al. 2003; Sneden et al. 2009), and HE 1523-0901 (blue, Frebel et al. 2007). All abundances are computed under the assumption of LTE. The Solar *r*-process decomposition of Arlandini et al. (1999) is shown as a reference (black line). *Lower panel:* Abundance differences between CS 29497-004 and the other *r*-II stars (normalised at Ce).

OH molecular line. Detections of Pt for other *r*-II stars would be most welcome to investigate the abundance of this third-peak element, and to validate the use of the 3301 Å line (conveniently located in the near-UV part of the spectrum accessible from the ground) to measure its abundance.

*Lead* is a particularly important element, as  $^{208}\text{Pb}$  is the end-point of many decay chains from heavier unstable products of the *r*-process, including Th and U. However, in the actinide-boost star CS 31082-001, Plez et al. (2004) measured a Pb abundance that is *lower* by some 0.4 dex than both the scaled-Solar *r*-process fraction of Pb (e.g.,  $\log \epsilon(\text{Pb}/\text{Eu}) = +0.62$  in Bisterzo et al. 2014), or the *r*-process model predictions: the theoretical waiting-point approximation *r*-process model of (Kratz et al. 2007) predicts an initial production of  $\log \epsilon(\text{Pb}/\text{Eu})_0 = +0.61$ , which, after about 13 Gyrs of decay of radioactive nuclei, adds up to  $\log \epsilon(\text{Pb}/\text{Eu}) = +0.70$  (see discussion in Roederer et al. 2009). The upper limit for Pb derived by Frebel et al. (2007) in HE 1523-0901 also implied a ratio of Pb relative to second- and third-peak *r*-process elements that was significantly lower than the *r*-process predictions, and commensurate with the measurement for CS 31082-001 (Plez et al. 2004). On the other hand, the upper limit for Pb derived for CS 22892-052 (Roederer et al. 2009) is fully compatible with a scaled-Solar *r*-process. At these low metallicities ( $[\text{Fe}/\text{H}] < -2.5$ ), these three stars were the only *r*-process-element dominated stars for which a measurement or

significant upper limit of Pb had been obtained (see the large sample and compilation by Roederer et al. 2010).

More recently, Mashonkina et al. (2012) computed NLTE Pb abundances for cool metal-poor stars, and showed that the NLTE corrections are sizable for the Pb I line used in metal-poor giants, such as the above *r*-II stars, unlike NLTE corrections for the second-peak *r*-process element Eu II, which experiences little departure from NLTE (to be expected for most elements measured from ionized species). In particular, Mashonkina et al. (2012) revised the Pb abundances for CS 31082-001 to  $\log \epsilon(\text{Pb}/\text{Eu})_{\text{NLTE}} = 0.67$ , and reported an actual detection of Pb for HE 1523-0901 of  $\log \epsilon(\text{Pb}/\text{Eu})_{\text{NLTE}} = 0.68$  (to be compared to  $\log \epsilon(\text{Pb}/\text{Eu})_{\text{LTE}} = 0.28$ ). These new NLTE values now compare remarkably well with the theoretical waiting-point approximation *r*-process model for a 13 Gyr old star (Kratz et al. 2007; Roederer et al. 2009),  $\log \epsilon(\text{Pb}/\text{Eu}) = +0.60$ , or the Solar *r*-process decomposition of Bisterzo et al. (2014),  $\log \epsilon(\text{Pb}/\text{Eu}) = +0.62$ .

The tentative detection of Pb presented here allows us to add CS 29497-004 to this picture, albeit with a rather large uncertainty. The most probable LTE Pb abundance for CS 29497-004 yields  $\log \epsilon(\text{Pb}/\text{Eu})_{\text{LTE}} = +0.41 \pm 0.3$  (while the conservative upper limit is  $< +0.91$ ), to which we apply a NLTE correction of +0.55 based on Mashonkina et al. (2012) (their Table 1, assuming the NLTE correction for their *r*-process enriched star with  $T_{\text{eff}}=5000\text{K}$ ,  $\log g=1.5$  and  $[\text{Fe}/\text{H}]=-3.0$ ), lead-

**Table 5.** Abundances of the neutron-capture elements for CS 29497-004. Column  $\sigma_m$  reports errors on the [Th/X] ratios propagated from stellar parameter uncertainties, and  $\sigma_t$  is the total error on the [Th/X] ratio (combining the observational uncertainty and  $\sigma_m$ ).

Z	Species	$\log \epsilon_\odot$	$\log \epsilon$	$\sigma$	$N_{\text{lines}}$	$\sigma_m$	$\sigma_t$
38	Sr II	2.97	0.76	0.11	4	0.07	0.11
39	Y II	2.24	-0.04	0.11	13	0.06	0.08
40	Zr II	2.60	0.63	0.14	27	0.04	0.07
41	Nb II	1.42	-0.33	0.00	1	0.01	0.07
42	Mo I	1.92	0.15	0.00	1	0.13	0.14
44	Ru I	1.84	0.61	0.04	5	0.13	0.15
45	Rh I	1.12	-0.18	0.12	2	0.13	0.16
46	Pd I	1.69	0.25	0.23	5	0.13	0.18
47	Ag I	1.24	-0.42	0.11	2	0.13	0.17
56	Ba II	2.13	0.35	0.17	5	0.08	0.12
57	La II	1.17	-0.38	0.14	13	0.05	0.08
58	Ce II	1.58	-0.19	0.12	31	0.02	0.06
59	Pr II	0.71	-0.67	0.04	6	0.02	0.06
60	Nd II	1.50	-0.02	0.09	33	0.02	0.07
62	Sm II	1.01	-0.30	0.11	17	0.01	0.06
63	Eu II	0.51	-0.66	0.04	7	0.02	0.06
64	Gd II	1.12	-0.31	0.12	20	0.03	0.07
65	Tb II	0.35	-1.08	0.07	9	0.02	0.06
66	Dy II	1.14	-0.08	0.07	21	0.03	0.07
67	Ho II	0.51	-0.76	0.04	3	0.15	0.17
68	Er II	0.93	-0.29	0.11	9	0.08	0.11
69	Tm II	0.15	-1.18	0.05	6	0.05	0.08
70	Yb II	1.08	-0.22	0.06	2	0.17	0.20
71	Lu II	0.06	-0.72	0.00	1	0.02	0.11
72	Hf II	0.88	-0.64	0.07	9	0.02	0.07
76	Os I	1.45	0.41	0.10	5	0.10	0.12
77	Ir I	1.35	0.23	0.02	2	0.06	0.09
78	Pt I	1.80	0.00	0.00	1	0.06	0.21
82	Pb I	1.95	-0.25	0.00	1	0.10	0.32
82	Pb I	1.95	< 0.25	0.00	1	0.10	0.32
90	Th II	0.09	-1.16	0.13	6	0.00	0.08
92	U II	0.50	-2.20	0.00	1	0.01	0.32

ing to  $\log \epsilon(\text{Pb}/\text{Eu})_{\text{NLTE}} = +0.96 \pm 0.3$ . This is consistent, within errorbars, with the Pb/Eu ratios in the two other  $r$ -II stars where Pb has been detected, CS 31082-001 and HE 1523-0901.

Obtaining precise Pb measurements for additional  $r$ -II stars (with and without actinide boosts) would clearly be required to better understand the nature of the  $r$ -process. One would indeed expect that the actinide excess in actinide-boost stars should *increase* its lead content with respect to “normal”  $r$ -II stars, owing to the enhanced contribution of decaying radioactive actinide nuclei to the Pb abundance over the lifetime of the star.

Interestingly, at higher metallicities ( $[\text{Fe}/\text{H}] \sim -2.2$  to  $-1.4$ ), the reanalysis of the Roederer et al. (2010) sample in NLTE by Mashonkina et al. (2012) found that, over that entire metallicity range, the Pb/Eu ratio is significantly higher than for the  $r$ -II stars discussed above (CS 31082-001, HE 1523-0901, and CS 29497-004), and displays a steady increase (albeit with some dispersion) towards the Solar Pb/Eu, which is reached around  $[\text{Fe}/\text{H}] \sim -1.4$ . The Pb/Eu ratio in  $r$ -II stars is assumed to be the  $r$ -process yield value, and the steady increase at higher metallicities is taken as due to early  $s$ -process enrichment. In this context, obtaining more Pb/Eu measurements in low-metallicity stars ( $r$ -II,  $r$ -I, and  $r$ -normal stars) would lead to improved understanding of the earliest phases of  $s$ -process enrichment. In particular, do  $r$ -normal stars with metallicities below  $[\text{Fe}/\text{H}] = -2.5$  also show a pure  $r$ -process Pb/Eu ratio? Although this would surely be a challenging measurement, it would also provide significant constraints.

### 5.3. Age determinations

We have determined nucleo-chronometric ages for CS 29497-004, using various combinations of chronometers involving Th and U and production ratios (hereafter PRs) from two parameterized nucleosynthesis models developed to reproduce the full distribution of the Solar System  $r$ -process “residuals” ( $N_{r,\odot} = N_\odot - N_{s,\odot}$ ): (i) the historical, largely site-independent “waiting-point” (WP) approach (see, e.g. Burbidge et al. 1957; Kratz et al. 1993, 2007), and (ii) the more recent, site-specific fully dynamical network calculations of the high-entropy-wind (HEW) of core-collapse supernovae (see, e.g. Woosley et al. 1994; Freiburghaus et al. 1999; Farouqi et al. 2010).

#### 5.3.1. $r$ -process production ratios (PRs)

The WP model used here is based on the historical assumption of an initial Fe seed, and furthermore a combination of  $(n, \gamma) - (\gamma, n)$  and  $\beta$ -flow equilibria at high neutron densities ( $10^{20} < n_n < 10^{28}$ ) at a fixed temperature ( $T_9 = 1.35$ ), and an instantaneous freezeout. As discussed in detail in Kratz et al. (1993), in principle a superposition of only three correlated components of neutron densities ( $n_n$ ) and nucleosynthesis time scales ( $\tau_r$ ) to independently fit the three  $N_{r,\odot}$  abundance peaks at  $A \sim 80, 130$ , and 195 was required to reproduce the full abundance pattern in nature. An updated version of this model (in terms of a finer  $n_n - \tau_r$  grid and an improved nuclear-physics input) from Kratz et al. (2007) is used for the age determinations presented in Table 6.

A more recent, still commonly used  $r$ -process model applied here, involves the so-called neutrino or high-entropy wind (HEW) from Type II (core-collapse) supernovae (ccSN; see, e.g., Woosley et al. 1994). In the calculations used for the present chronometric age determinations, we follow the description of adiabatically expanding mass zones at the outermost neutron star layers, as initially utilized in Freiburghaus et al. (1999). After several updates of both the detailed dynamical simulations, as well as the theoretical and experimental nuclear-data input, we use here the version explained in great detail in Farouqi et al. (2010). After a charged-particle freezeout leading to a neutron-rich *seed* composition beyond the historically assumed Fe peak and even beyond the  $N = 50$  magic shell, the expanding mass zones have different initial entropies ( $S$ ), so that in the HEW model the overall ejected  $r$ -process matter represents a superposition of entropies. The ratio of free neutrons to *seed* nuclei ( $Y_n/Y_{\text{seed}}$ ) is correlated to the three main parameters of the HEW, i.e. the electron abundance ( $Y_e = Z/A$ , which defines the *neutron richness* of the  $r$ -ejecta), the entropy  $S$  and the expansion velocity of the ejecta ( $Y_{\text{exp}}$ ); and can be expressed by a simple  *$r$ -process strength* formula  $Y_n/Y_{\text{seed}} \sim V_{\text{exp}}(S/Y_e)^3$ . Within this parameter space, it became immediately evident that the ccSN - HEW model predicts two clearly different primary, rapid nucleosynthesis modes with three different components: at low entropies ( $S < 50$ ) a neutron-rich charged-particle component without free neutrons, for somewhat higher entropies ( $50 < S < 150$ ) a *weak* neutron-capture  $r$ -process, and for high entropies ( $S > 150$ ) a robust Solar System-like *main*  $r$ -process, which we need here for our age determinations (for details, see Kratz et al. 2008; Farouqi et al. 2009a,b, 2010). Initially, as in the case of the WP approach, purposively chosen to closely reproduce the full  $N_{r,\odot}$  abundance pattern, a parameter combination of  $Y_e = 0.45, V_{\text{exp}} = 7500 \text{ km/s}$  and an entropy range of  $10 < S < 280$  was chosen to compare our HEW predictions to recent astronomical observations (see, e.g. Farouqi et al. 2009a; Hayek et al. 2009; Farouqi et al. 2010; Kratz et al. 2014).

**Table 6.** Age determinations for CS 29497-004, using initial production ratios from: (1)  $\log(\text{PR})_{\text{HEW}}$ : HEW predictions (this paper) for  $Y_e = 0.447^{+0.002}_{-0.002}$  based on (Farouqi et al. 2010), (2)  $\log(\text{PR}_{\text{WP1}})$  and (3)  $\log(\text{PR}_{\text{WP2}})$ : waiting-point assumption model predictions (from Kratz et al. 2007, their Table 2, columns 6 and 3 resp). Errors on ages are evaluated in two different ways: the  $Y_e$  variations on PRs are propagated into  $\text{Age}_{\text{HEW}}$  as super- and sub-scripts, while  $\text{ErrAge}_{\text{obs}}$  reports the observational error propagated from the observational uncertainties on the abundance ratio. For mean ages, the dispersion around the mean is also given in the corresponding age column.

X/Y	$\log \epsilon(\text{X/Y})_{\text{obs}}$	$\text{ErrAge}_{\text{obs}}$	$\log(\text{PR})_{\text{HEW}}$	$\text{Age}_{\text{HEW}}$ (1)	$\log(\text{PR}_{\text{WP1}})$	$\text{Age}_{\text{WP1}}$ (2)	$\log(\text{PR}_{\text{WP2}})$	$\text{Age}_{\text{WP2}}$ (3)
		[Gyr]		[Gyr]		[Gyr]		[Gyr]
Th/Ba	$-1.51 \pm 0.12$	5.7	$-1.058^{0.103}_{-0.091}$	$21.11^{4.81}_{-4.25}$				
Th/La	$-0.78 \pm 0.08$	3.9	$-0.362^{0.105}_{-0.093}$	$19.52^{4.90}_{-4.34}$				
Th/Ce	$-0.97 \pm 0.06$	3.0	$-0.724^{0.100}_{-0.091}$	$11.49^{4.67}_{-4.25}$				
Th/Pr	$-0.49 \pm 0.06$	3.0	$-0.313^{0.099}_{-0.092}$	$8.27^{4.60}_{-4.27}$				
Th/Nd	$-1.14 \pm 0.07$	3.0	$-0.928^{0.097}_{-0.092}$	$9.90^{4.53}_{-4.30}$				
Th/Sm	$-0.86 \pm 0.06$	3.0	$-0.796^{0.100}_{-0.090}$	$2.99^{4.67}_{-4.20}$				
Th/Eu	$-0.50 \pm 0.06$	3.0	$-0.240^{0.104}_{-0.092}$	$12.14^{4.86}_{-4.30}$	-0.375	5.8	-0.276	10.5
Th/Gd	$-0.85 \pm 0.07$	3.2	$-0.569^{0.105}_{-0.093}$	$13.12^{4.90}_{-4.34}$				
Th/Dy	$-1.08 \pm 0.07$	3.1	$-0.827^{0.105}_{-0.094}$	$11.82^{4.90}_{-4.39}$				
Th/Ho	$-0.40 \pm 0.17$	8.1	$-0.071^{0.109}_{-0.046}$	$15.36^{5.09}_{-2.15}$				
Th/Er	$-0.87 \pm 0.11$	4.9	$-0.592^{0.107}_{-0.096}$	$12.98^{5.00}_{-4.48}$				
Th/Tm	$0.02 \pm 0.08$	3.9	$+0.155^{0.106}_{-0.095}$	$6.31^{4.95}_{-4.44}$				
Th/Hf	$-0.52 \pm 0.07$	3.0	$-0.036^{0.107}_{-0.093}$	$22.60^{5.00}_{-4.34}$	-0.335	8.6	-0.063	21.3
Th/REE	weighted mean (rms)	3.5		11.99( $\pm 5.46$ )				
Th/Os	$-1.57 \pm 0.12$	5.7	$-0.917^{0.096}_{-0.087}$	$30.50^{4.48}_{-4.06}$	-1.125	20.8	-1.009	26.2
Th/Ir	$-1.39 \pm 0.09$	4.1	$-0.839^{0.097}_{-0.089}$	$25.73^{4.53}_{-4.16}$	-1.153	11.1	-1.022	17.2
Th/Pt	$-1.16 \pm 0.22$	10.1	$-1.112^{0.069}_{-0.065}$	$2.24^{3.22}_{-3.04}$	-1.444	-13.3	-1.585	-19.9
Th/(Os,Ir)	weighted mean (rms)	4.7		27.35( $\pm 2.26$ )		14.4( $\pm 4.6$ )		20.2( $\pm 4.3$ )
Th/(Os,Ir,Pt)	weighted mean (rms)	5.4		24.92( $\pm 7.74$ )				
Th/U	$-1.04 \pm 0.30$	6.6	$0.283^{0.011}_{-0.013}$	$16.50^{0.24}_{-0.28}$	+0.195	18.4	+0.192	18.5
U/Ba	$-2.55 \pm 0.32$	4.8	$-1.341^{0.114}_{-0.104}$	$17.94^{1.69}_{-1.54}$				
U/La	$-1.82 \pm 0.31$	4.6	$-0.645^{0.116}_{-0.106}$	$17.44^{1.72}_{-1.57}$				
U/Ce	$-2.01 \pm 0.30$	4.5	$-1.007^{0.111}_{-0.104}$	$14.88^{1.65}_{-1.54}$				
U/Pr	$-1.53 \pm 0.30$	4.5	$-0.596^{0.110}_{-0.105}$	$13.86^{1.63}_{-1.55}$				
U/Nd	$-2.18 \pm 0.30$	4.5	$-1.211^{0.108}_{-0.105}$	$14.38^{1.60}_{-1.56}$				
U/Sm	$-1.90 \pm 0.30$	4.5	$-1.079^{0.111}_{-0.103}$	$12.18^{1.65}_{-1.53}$				
U/Eu	$-1.54 \pm 0.30$	4.5	$-0.523^{0.115}_{-0.105}$	$15.09^{1.71}_{-1.59}$	-0.570	14.4	-0.468	15.9
U/Gd	$-1.89 \pm 0.30$	4.5	$-0.852^{0.116}_{-0.106}$	$15.40^{1.72}_{-1.57}$				
U/Dy	$-2.12 \pm 0.30$	4.5	$-1.110^{0.116}_{-0.107}$	$14.99^{1.72}_{-1.59}$				
U/Ho	$-1.44 \pm 0.34$	5.1	$-0.354^{0.120}_{-0.059}$	$16.12^{1.78}_{-0.88}$				
U/Er	$-1.91 \pm 0.31$	4.6	$-0.875^{0.118}_{-0.109}$	$15.36^{1.75}_{-1.62}$				
U/Tm	$-1.02 \pm 0.31$	4.6	$-0.128^{0.117}_{-0.108}$	$13.24^{1.74}_{-1.60}$				
U/Hf	$-1.56 \pm 0.30$	4.5	$-0.319^{0.118}_{-0.106}$	$18.42^{1.75}_{-1.57}$	-0.530	15.3	-0.356	19.4
U/REE	weighted mean (rms)	4.6		15.29( $\pm 1.74$ )				
U/Os	$-2.61 \pm 0.32$	4.7	$-1.200^{0.107}_{-0.100}$	$20.92^{1.59}_{-1.48}$	-1.320	19.1	-1.201	20.9
U/Ir	$-2.43 \pm 0.31$	4.6	$-1.122^{0.108}_{-0.102}$	$19.41^{1.60}_{-1.51}$	-1.348	16.1	-1.215	18.0
U/Pt	$-2.20 \pm 0.37$	5.4	$-1.395^{0.080}_{-0.078}$	$11.90^{1.19}_{-1.19}$	-1.639	8.3	-1.777	6.3
U/(Os,Ir)	weighted mean (rms)	4.6		20.14( $\pm 0.75$ )		15.1( $\pm 4.3$ )		19.4( $\pm 1.4$ )
U/(Os,Ir,Pt)	weighted mean (rms)	4.9		17.94( $\pm 3.69$ )		17.5( $\pm 1.5$ )		15.9( $\pm 6.0$ )

This approach seemed to be justified for quite some time in the past, because the striking similarity between the  $N_{r,\odot}$  abundances above Ba (in fact already above Te, see Roederer et al. 2012) with the pattern observed in the EMP  $r$ -II star CS 22892-052 (Sneden et al. 1996, 2003), has led to the conclusion that every astrophysical event will produce such a “unique” Solar-like pattern. However, more recently the observations of several so-called actinide-boost stars (such as CS 31082-001 (Hill et al. 2002; Barbuy et al. 2011; Siqueira Mello et al. 2013), or HE 2252-4225 (Mashonkina et al. 2014)), and the  $r$ -process

ubiquity study of Roederer et al. (2010), have questioned this assumption. Therefore, motivated by these observations, and our failure to obtain a consistent mean age for the Th/X and U/X chronometer pairs over the entire Solar-like rare earth elements and third-peak region, we have extended our HEW age determinations from the initial constant  $Y_e - V_{\text{exp}} - S$  parameter assumption to variations of the  $Y_e$  parameter. With this, we are changing the neutron richness of the  $r$ -process ejecta, to represent the diversity of observed  $r$ -process. And indeed, with optimized values of  $Y_e < 0.45$  we have been able to obtain more consistent



mean chronometric age. For example, for  $r$ -II stars showing an actinide boost (e.g., CS 31082-001), we can thus avoid the unphysical negative age for Th/Eu that was derived when using PRs reproducing the Solar System  $r$ -process. In the present case of CS 29497-004, we have been able to obtain consistent mean Th/X, U/X and Th/U ages for a slightly lower electron fraction  $Y_e \sim 0.447(\pm 0.002)$ , i.e., for HEW ejecta that are more neutron rich than required to fit the standard  $N_{r,\odot}$  ones.

The resulting ages are listed in Table 6, where the HEW model PRs and ages are given in columns (1) and the WP approach are reported in columns (2) and (3) as in Kratz et al. (2007). The age uncertainties ( $\text{ErrAge}_{\text{obs}}$ ) listed in this table take into account the observational errors – that is, the uncertainties in the determination of the abundance ratios, including measurement errors and (random) errors of stellar parameters ( $T_{\text{eff}}$  and  $\log g$ ). Uncertainties associated to the assumed set of PRs are explored both by comparing HEW and WP models, and through the exploration of different  $Y_e$  within the HEW model (reported as super- and sub-scripts for lower and upper uncertainties on the  $\text{PR}_{\text{HEW}}$  and corresponding  $\text{Age}_{\text{HEW}}$  columns). Comparing age uncertainties arising from PRs to  $\text{ErrAge}_{\text{obs}}$  in this table, it can be appreciated that, while for Th based ratios, the two sources have comparable amplitudes, the observational uncertainty always dominates chronometers involving U.

### 5.3.2. WP approximation model ages

Table 6 also presents ages derived using PRs from (Kratz et al. 2007) based on  $r$ -process calculations using Fe seeds. In column (3) we report the theoretical production ratio results that yield the best overall fit to the Solar System  $r$ -process abundance data for masses  $A > 83$ , while in column (2) we report the ratios of theoretical production of Th and U to the present-day *observed* Solar System  $r$ -process elemental abundances (see Kratz et al. 2007, for a detailed description of column 6 of their Table 2). These ages display the same basic features as the HEW PRs, namely older ages when U is used rather than Th, in combination with any of the rare earths, but still commensurate within uncertainties. We further note that PRs computed with respect to present-day Solar System elemental abundances (col. 2) yield ages that are, on average, lower by 7.2 Gyr for Th-based and 2.3 Gyr for U-based chronometers than those using purely theoretical PRs (col. 3). With these PRs computed with respect to present-day Solar System elemental abundances, the weighted mean age for CS 29497-004 is 12.2 Gyr, with a dispersion around the mean of  $\sigma = 4.9$  Gyr, and a formal (observational) error of 3.6 Gyr.

### 5.3.3. HEW-model ages

The weighted average of the age determinations for CS 29497-004 using the ratios of Th to 12 rare-earth species (Ba, La, Ce, Pr, Nd, Sm, Eu, Gd, Dy, Ho, Er, Tm) and the HEW PRs with  $Y_e = 0.447$  is 12.0 Gyr, with a weighted dispersion around the mean of  $\sigma = 5.4$  Gyr, and a formal (observational) error of 3.5 Gyr. The weighted average age using the ratios of U to the rare-earth ratios is somewhat higher: 15.3 Gyr, with a significantly lower weighted dispersion around the mean of  $\sigma = 1.7$  Gyr, and a formal (observational) error of 4.6 Gyr. The observational age uncertainty is in both cases due mostly to the observational uncertainty on the Th (or U) abundance itself, and for U-based chronometers, observational uncertainties largely exceed uncertainties due to PRs. These two mean ages are therefore both fully compatible with each other, and with the accepted

age of the Universe of  $13.772 \pm 0.059$  Gyr (Bennett et al. 2013). The Th/U chronometer pair alone yields an age of 16.5 Gyr with an associated observational uncertainty of 6.6 Gyr, again fully compatible with the age of the Universe. The combined age of CS 29497-004 from all these chronometer pairs is 13.7 Gyr, with a formal (observational) error of 4.4 Gyr. The low scatter around the mean age from the ratios of U to the rare earths indicates that the production ratios for these elements are well-predicted by the HEW model. The chronometer pairs using the heaviest detected second-peak element Hf and the third-peak element Os provide significantly higher ages, hinting at possible Hf and Os over-production in the HEW model.

As outlined in section 5.3.1, the theoretical predictions of the PRs of the relevant chronometer pairs also suffer uncertainties linked to the many flavours of  $r$ -process that can arise in astrophysical sites, for example linked to the neutron richness of the ejecta. To quantify this effect, we tabulated in Table 6 PRs arising from the HEW model with different  $Y_e$  (given as lower and upper uncertainties to PRs) for each chronometer pair (Th to each of the Rare Earth Elements -hereafter REE-, U to REE elements, U/Th, etc.). Fig. 15 shows how ages react as a function of  $Y_e$ . Because the slope of the age vs.  $Y_e$  is different for different chronometer pairs (e.g., Th/REE, U/REE, and U/Th), it is in principle possible to determine the best fitting  $Y_e$  for a given star. For CS 29497-004, all  $Y_e$  explored here are allowed, and both the chosen  $Y_e = 0.447$  or  $Y_e = 0.445$  allow an excellent agreement for the age of different chronometer pairs.

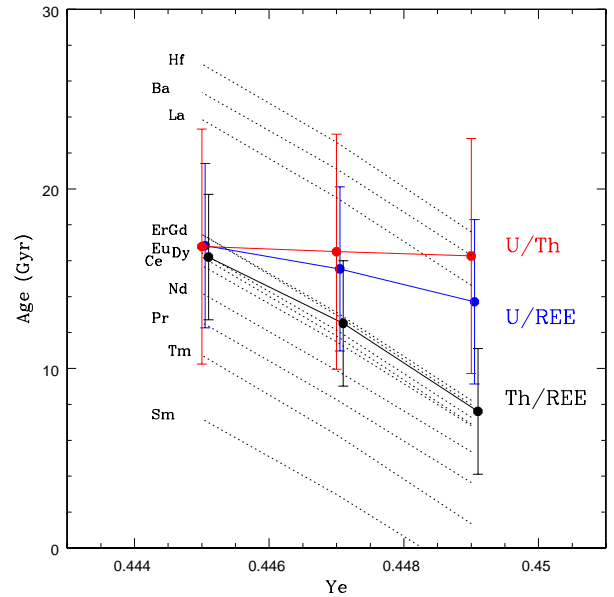


**Fig. 15.** Ages for CS 29497-004 as a function of the assumed neutron richness ( $Y_e$ ) in the HEW model: weighted mean of Th/X ages for 12 rare-earth elements (black circles and full line); weighted mean of U/X ages for 12 rare-earth elements (blue circles and full line); U/Th age (red circles and full line). The black dotted line depict Th/X ages for the individual elements. Weights are used to take into account the observational error on abundance ratios.

Comparing PRs and ages obtained through various methods, as is done in Table 6 by comparing the HEW and waiting-point approximation PRs, also allows to gain insight on the robustness of theoretical predictions. For the ratios for which all three PRs are available, the variation among PRs is lower than the



observational uncertainty for all pairs involving U (Th/U, U/Eu, U/Os, U/Ir, U/Pt) except U/Hf, while the variation among the PR sources is larger than the observational uncertainty for pairs involving the Th chronometer alone (Th/Eu, Th/Hf, Th/Os, Th/Ir, Th/Pt). Most remarkable is the agreement obtained for Th/U, confirming that this ratio is a robust chronometer even in the face of PR uncertainties (e.g., Goriely & Arnould 2001; Hill et al. 2002; Wanajo et al. 2002). Fig. 15 illustrates again the robustness of the Th/U chronometer pair, as the production ratios of these two elements move in lockstep when physical conditions change.

Finally, we note that the very low Pt abundance in CS 29497-004 leads to exceedingly low (and even unphysical) ages when used as a reference element for both of the Th or U chronometer pairs, which we suspect is likely due to a systematic offset of our Pt measurement.

## 6. Discussion and conclusions

The discovery of *r*-II stars has proceeded slowly since their first recognition over twenty years ago. There now exist a total of about 25 *r*-II stars that have been identified among stars of the Galactic halo population, but only three (now including CS 29497-004) have confident detections of U. The majority of the remaining *r*-II stars have measurements of Th available as well. One additional halo *r*-II star with detected U (and Th) has been found from high-resolution spectroscopic follow-up of VMP/EMP stars from the RAVE survey (Steinmetz et al. 2006), as reported by Placco et al. (in prep.). Although it is clearly desirable to dramatically increase the numbers of known *r*-II stars (efforts to accomplish this goal are presently underway), the extant sample already allows a number of broad conclusions to be reached.

- ***r*-II stars are found in all evolutionary stages:** Until recently, all of the recognized *r*-II stars were giants, leaving open the possibility that there exists some form of peculiarity that could account for this enhancement specifically in red-giant stellar atmospheres (see, e.g., Sneden et al. 2008). The identification of SDSS J2357-0052 as a cool main-sequence *r*-II star by Aoki et al. (2010) removed much of this concern. Even more recently, Roederer et al. (2014a) identified a total of nine new highly *r*-process-enhanced stars from the HK survey (a mix of *r*-I and *r*-II stars) in the subgiant and horizontal-branch stages of evolution, confirming that this phenomenon occurs in all stages, and almost certainly arose due to pollution of the natal gas from which the *r*-II and *r*-I stars formed by progenitor(s) that produced copious amounts of *r*-process elements.
- ***r*-II stars that exhibit an actinide boost:** As shown in paper X of this series (Mashonkina et al. 2014), on the order of 30% of *r*-II stars exhibit substantially higher abundances of Th (and U, where it is observed) relative to stable *r*-process elements such as Eu (by  $\sim 0.3 - 0.4$  dex) compared to the majority of *r*-II stars. This so-called actinide-boost phenomenon has not yet been accounted for by models for the progenitors that created the *r*-process, but it remains, in our view, a strong potential constraint, in particular if a single class of progenitors are ultimately identified with the origin of *r*-process elements. They must be capable of, about one-third of the time, producing this *obvious* abundance anomaly. Clearly, refinement of the observed frequency of actinide-boost stars among highly *r*-process-element

enhanced stars is desired.

- **Contrast in the first-peak *r*-process elements among *r*-I and *r*-II stars:** Siqueira Mello et al. (2014) have carried out a detailed comparison of the first-peak (e.g., Sr, Y, Zr) relative to the second-peak (e.g., Ba, La, Eu) elements for known *r*-I and *r*-II stars, concluding that the first-peak elements (generally associated with the weak *r*-process) are enhanced in the *r*-I stars relative to those observed in the *r*-II stars. In other words, the weak *r*-process signature observed in *r*-normal and *r*-I stars is drowned in the excess of main *r*-process that define the *r*-II class. Although confirmation of this result awaits determinations of the abundance patterns for a larger number of *r*-process-enhanced stars, these authors suggest that this could be interpreted as evidence that different nucleosynthesis pathways (hence different progenitor sites) are responsible for the different sub-classes of *r*-process-enhanced stars.
- **Rejection of binary mass-transfer scenarios associated with *r*-process enhancement:** Previously suggested models for the production of enhancements in *r*-process elements for a small fraction of VMP/EMP stars considered the possibility that these arose from mass-transfer events (via wind accretion) associated with a companion star responsible for their creation (see, e.g., Wanajo et al. 2006, and references therein). Limited radial-velocity monitoring campaigns were unable to reject these models for a number of *r*-II stars, including the prototypical star CS 22892-052 (e.g., Preston & Sneden 2001). The results of a more extensive radial-velocity monitoring program (based on far more accurate measurements than were previously available) for *r*-process-enhanced stars, reported by Hansen et al. (2015), have demonstrated convincingly that the chemical peculiarities of the *r*-II and *r*-I stars cannot be generally caused by binary companions. The binary fraction of such stars was shown by these authors to be  $18 \pm 11\%$  (3 of 17 stars), completely consistent with the observed binary fractions of chemically “normal” VMP and EMP stars. Instead, as these authors concluded, the *r*-process enhancement was imprinted on the natal molecular clouds of these stars by an external source.

Our study of the third *r*-II star with detected U, CS 29497-004, an object that does not exhibit an actinide boost, has enabled new estimates of the radioactive-decay age for *r*-II stars, albeit with larger than desired errors arising due to the difficulty of obtaining accurate abundances for chronometers involving U for this relatively faint ( $V = 14$ ) and comparatively warm ( $T_{\text{eff}} = 5000$  K) star. We have also obtained a tentative detection of Pb for this star, and called attention to the important role this element plays in providing constraints on the nature of the *r*-process, and the rise of the *s*-process. We look forward to the refinement of our understanding expected from the identification of additional *r*-process-enhanced stars with detected Pb, Th, and U, both with and without actinide boosts, based on newly initiated surveys of (in particular *bright*;  $9 < V < 14$ ) VMP and EMP stars now underway.

**Acknowledgements.** We are grateful to the ESO staff at Paranal and Garching for obtaining the observations and reducing the data, respectively. N.C. expresses his gratitude to the Observatoire Paris-Meudon for hospitality shown to him during a 1-month visit during which most of this paper was written. He acknowledges support by Sonderforschungsbereich SFB 881 “The Milky Way System” (subproject A4) of the German Research Foundation (DFG). T.C.B. acknowledges partial support for this work from grants PHY 02-16783, PHY 08-22648;

Physics Frontier Center/Joint Institute for Nuclear Astrophysics (JINA), and PHY 14-30152; Physics Frontier Center/JINA Center for the Evolution of the Elements (JINA-CEE), awarded by the US National Science Foundation. P.S.B. is a Research Fellow of the Royal Swedish Academy of Sciences supported by a grant from the Knut and Alice Wallenberg Foundation.

## References

- Alonso, A., Arribas, S., & Martínez-Roger, C. 1999, *A&AS*, 139, 335
- Alvarez, R. & Plez, B. 1998, *A&A*, 330, 1109
- Andrievsky, S. M., Spite, M., Korotin, S. A., et al. 2008, *A&A*, 481, 481
- Aoki, W., Beers, T. C., Honda, S., & Carollo, D. 2010, *ApJ*, 723, L201
- Arlandini, C., Käppeler, F., Wisshak, K., et al. 1999, *ApJ*, 525, 886
- Asplund, M. 2005, *ARA&A*, 43, 481
- Asplund, M., Grevesse, N., & Sauval, A. 2005, in *ASP Conf. Ser.*, Vol. 336, *Cosmic Abundances as Records of Stellar Evolution and Nucleosynthesis in honor of David L. Lambert*, ed. F. Bash & T. Barnes, San Francisco, 25–38
- Asplund, M., Gustafsson, B., Kiselman, D., & Eriksson, K. 1997, *A&A*, 318, 521
- Barbuy, B., Spite, M., Hill, V., et al. 2011, *A&A*, 534, A60
- Barklem, P. S., Christlieb, N., Beers, T. C., et al. 2005, *A&A*, 439, 129, (Paper II)
- Beers, T. C. & Christlieb, N. 2005, *ARA&A*, 43, 531
- Beers, T. C., Flynn, C., Rossi, S., et al. 2007, *ApJ Suppl.*, 168, 128
- Beers, T. C., Preston, G. W., & Shectman, S. A. 1985, *AJ*, 90, 2089
- Beers, T. C., Preston, G. W., & Shectman, S. A. 1992, *AJ*, 103, 1987
- Bennett, C. L., Larson, D., Weiland, J. L., et al. 2013, *ApJS*, 208, 20
- Biemont, E., Grevesse, N., Hannaford, P., & Lowe, R. M. 1981, *ApJ*, 248, 867
- Biemont, E., Grevesse, N., Kwiatkowski, M., & Zimmermann, P. 1984, *A&A*, 131, 364
- Bisterzo, S., Travaglio, C., Gallino, R., Wiescher, M., & Käppeler, F. 2014, *ApJ*, 787, 10
- Burbidge, E. M., Burbidge, G. R., Fowler, W. A., & Hoyle, F. 1957, *Reviews of Modern Physics*, 29, 547
- Cameron, A. G. W. 1957, *PASP*, 69, 201
- Cayrel, R., Depagne, E., Spite, M., et al. 2004, *A&A*, 416, 1117
- Cayrel, R., Hill, V., Beers, T., et al. 2001, *Nature*, 409, 691
- Christlieb, N., Beers, T. C., Barklem, P. S., et al. 2004, *A&A*, 428, 1043, (Paper I)
- Collet, R., Asplund, M., & Trampedach, R. 2007, *A&A*, 469, 687
- Corliss, C. H. & Bozman, W. R. 1962, *Experimental transition probabilities for spectral lines of seventy elements; derived from the NBS Tables of spectral-line intensities*
- Cowan, J., Sneden, C., Burles, S., et al. 2002, *ApJ*, 572, 861
- Cowley, C. R. & Corliss, C. H. 1983, *MNRAS*, 203, 651
- Den Hartog, E. A., Lawler, J. E., Sneden, C., & Cowan, J. J. 2003, *ApJS*, 148, 543
- Dobrovolskas, V., Kučinskis, A., Steffen, M., et al. 2013, *A&A*, 559, A102
- Duquette, D. W. & Lawler, J. E. 1985, *Journal of the Optical Society of America B Optical Physics*, 2, 1948
- Edvardsson, B., Andersen, J., Gustafsson, B., et al. 1993, *A&A*, 275, 101
- Farouqi, K., Kratz, K.-L., Mashonkina, L. I., et al. 2009a, *ApJ*, 694, L49
- Farouqi, K., Kratz, K.-L., & Pfeiffer, B. 2009b, *PASA*, 26, 194
- Farouqi, K., Kratz, K.-L., Pfeiffer, B., et al. 2010, *ApJ*, 712, 1359
- Frebel, A., Christlieb, N., Norris, J. E., et al. 2007, *ApJ*, 660, L117
- Freiburghaus, C., Rembges, J.-F., Rauscher, T., et al. 1999, *ApJ*, 516, 381
- Goriely, S. & Arnould, M. 2001, *A&A*, 379, 1113
- Grevesse, N. 1969, *Sol. Phys.*, 6, 381
- Grevesse, N. & Sauval, A. J. 2000, in *Origin of Elements in the Solar System, Implications of Post-1957 Observations*, ed. O. Manuel, 261
- Gustafsson, B., Bell, R. A., Eriksson, K., & Nordlund, A. 1975, *A&A*, 42, 407
- Gustafsson, B., Edvardsson, B., Eriksson, K., et al. 2008, *A&A*, 486, 951
- Hannaford, P., Lowe, R. M., Biemont, E., & Grevesse, N. 1985, *A&A*, 143, 447
- Hansen, T. T., Andersen, J., Nordström, B., et al. 2015, *A&A*, 583, A49
- Hayek, W., Wiesendahl, U., Christlieb, N., et al. 2009, *A&A*, 504, 511
- Hill, V., Plez, B., Cayrel, R., et al. 2002, *A&A*, 387, 560
- Ishimaru, Y., Wanajo, S., & Prantzos, N. 2015, *ApJ*, 804, L35
- Ivarsson, S., Andersen, J., Nordström, B., et al. 2003, *A&A*, 409, 1141
- Ivarsson, S., Litzén, U., & Wahlgren, G. M. 2001, *Phys. Scr.*, 64, 455
- Ji, A. P., Frebel, A., Chiti, A., & Simon, J. D. 2016, *Nature*, 531, 610
- Kratz, K.-L., Bitouzet, J.-P., Thielemann, F.-K., Moeller, P., & Pfeiffer, B. 1993, *ApJ*, 403, 216
- Kratz, K.-L., Farouqi, K., Mashonkina, L. I., & Pfeiffer, B. 2008, *New Astronomy Review*, 52, 390
- Kratz, K.-L., Farouqi, K., & Möller, P. 2014, *ApJ*, 792, 6
- Kratz, K.-L., Farouqi, K., Pfeiffer, B., et al. 2007, *ApJ*, 662, 39
- Kupka, F., Piskunov, N., Ryabchikova, T. A., Stempels, H. C., & Weiss, W. W. 1999, *A&AS*, 138, 119
- Kupka, F. G., Ryabchikova, T. A., Piskunov, N. E., Stempels, H. C., & Weiss, W. W. 2000, *Baltic Astronomy*, 9, 590
- Kwiatkowski, M., Zimmermann, P., Biemont, E., & Grevesse, N. 1982, *A&A*, 112, 337
- Lai, D. K., Bolte, M., Johnson, J. A., et al. 2008, *ApJ*, 681, 1524
- Lawler, J. E., Bonvallet, G., & Sneden, C. 2001a, *ApJ*, 556, 452
- Lawler, J. E., Den Hartog, E. A., Sneden, C., & Cowan, J. J. 2006, *ApJS*, 162, 227
- Lawler, J. E., Hartog, E. A. D., Labby, Z. E., et al. 2007, *ApJS*, 169, 120
- Lawler, J. E., Sneden, C., & Cowan, J. J. 2004, *ApJ*, 604, 850
- Lawler, J. E., Sneden, C., Cowan, J. J., et al. 2008, *ApJS*, 178, 71
- Lawler, J. E., Wickliffe, M. E., Cowley, C. R., & Sneden, C. 2001b, *ApJS*, 137, 341
- Lawler, J. E., Wickliffe, M. E., den Hartog, E. A., & Sneden, C. 2001c, *ApJ*, 563, 1075
- Lodders, K., Palme, H., & Gail, H.-P. 2009, *Landolt Börnstein*
- Mårtensson-Pendrill, A.-M., Gough, D. S., & Hannaford, P. 1994, *Phys. Rev. A*, 49, 3351
- Mashonkina, L., Christlieb, N., Barklem, P. S., et al. 2010, *A&A*, 516, A46
- Mashonkina, L., Christlieb, N., & Eriksson, K. 2014, *A&A*, 569, A43, (Paper X)
- Mashonkina, L., Ryabtsev, A., & Frebel, A. 2012, *A&A*, 540, A98
- McWilliam, A. 1998, *AJ*, 115, 1640
- Migdalek, J. 1978, *J. Quant. Spec. Radiat. Transf.*, 20, 81
- Miles, B. M. & Wiese, W. L. 1969, *Atomic Data*, 1, 1
- Nilsson, H., Ivarsson, S., Johansson, S., & Lundberg, H. 2002a, *A&A*, 381, 1090
- Nilsson, H., Zhang, Z. G., Lundberg, H., Johansson, S., & Nordström, B. 2002b, *A&A*, 382, 368
- Palmeri, P., Quinet, P., Wyart, J.-F., & Biémont, E. 2000, *Phys. Scr.*, 61, 323
- Plez, B. 1992, *A&AS*, 94, 527
- Plez, B., Hill, V., Cayrel, R., et al. 2004, *A&A*, 428, L9
- Preston, G. & Sneden, C. 2001, *AJ*, 122, 1545
- Roederer, I. U., Cowan, J. J., Karakas, A. I., et al. 2010, *ApJ*, 724, 975
- Roederer, I. U., Cowan, J. J., Preston, G. W., et al. 2014a, *MNRAS*, 445, 2970
- Roederer, I. U., Kratz, K.-L., Frebel, A., et al. 2009, *ApJ*, 698, 1963
- Roederer, I. U., Lawler, J. E., Cowan, J. J., et al. 2012, *ApJ*, 747, L8
- Roederer, I. U., Mateo, M., Bailey, III, J. I., et al. 2016, *AJ*, 151, 82
- Roederer, I. U., Preston, G. W., Thompson, I. B., et al. 2014b, *AJ*, 147, 136
- Salih, S. & Lawler, J. E. 1985, *Journal of the Optical Society of America B Optical Physics*, 2, 422
- Serminato, A., Gallino, R., Travaglio, C., Bisterzo, S., & Straniero, O. 2009, *Publications of the Astronomical Society of Australia*, 26, 153
- Simmerer, J., Sneden, C., Cowan, J. J., et al. 2004, *ApJ*, 617, 1091
- Siqueira Mello, C., Hill, V., Barbuy, B., et al. 2014, *A&A*, 565, A93
- Siqueira Mello, C., Spite, M., Barbuy, B., et al. 2013, *A&A*, 550, A122
- Skrutskie, M. F., Cutri, R. M., Stiening, R., et al. 2006, *AJ*, 131, 1163
- Sneden, C., Cowan, J., Ivans, I., et al. 2000, *ApJ*, 533, L139
- Sneden, C., Cowan, J., Lawler, J., et al. 2003, *ApJ*, 591, 936
- Sneden, C., Cowan, J. J., & Gallino, R. 2008, *ARA&A*, 46, 241
- Sneden, C., Lawler, J. E., Cowan, J. J., Ivans, I. I., & Den Hartog, E. A. 2009, *ApJS*, 182, 80
- Sneden, C., McWilliam, A., Preston, G., et al. 1996, *ApJ*, 467, 819
- Sneden, C., Preston, G., McWilliam, A., & Searle, L. 1994, *ApJ*, 431, L27
- Spite, M., Cayrel, R., Hill, V., et al. 2006, *A&A*, 455, 291
- Spite, M., Cayrel, R., Plez, B., et al. 2005, *A&A*, 430, 655
- Steinmetz, M., Zwitter, T., Siebert, A., et al. 2006, *AJ*, 132, 1645
- Travaglio, C., Gallino, R., Arnone, E., et al. 2004, *ApJ*, 601, 864
- Travaglio, C., Gallino, R., Busso, M., & Gratton, R. 2001, *ApJ*, 549, 346
- Wanajo, S., Itoh, N., Ishimaru, Y., Nozawa, S., & Beers, T. 2002, *ApJ*, 577, 853
- Wanajo, S., Nomoto, K., Iwamoto, N., Ishimaru, Y., & Beers, T. C. 2006, *ApJ*, 636, 842
- Westin, J., Sneden, C., Gustafsson, B., & Cowan, J. 2000, *ApJ*, 530, 783
- Whaling, W. & Brault, J. W. 1988, *Phys. Scr.*, 38, 707
- Woosley, S. E., Wilson, J. R., Mathews, G. J., Hoffman, R. D., & Meyer, B. S. 1994, *ApJ*, 433, 229

## Appendix A: Individual radial velocity measurements for CS 29497-004

## Appendix B: Neutron-capture element linelist

Table B.1 reports the heavy elements linelist together with individual abundance measurements for CS 29497-004. References for log gf sources are given in column 5, as follows: 1: Sneden

**Table A.1.** Radial velocity data for CS 29497-004.

HJD	$v_{\text{rad}} \text{ km/s}$	$\sigma$
2452214.634255	105.023	0.502
2452549.624812	104.039	0.395
2452555.600435	104.173	0.271
2452582.517666	104.697	0.350
2452584.522592	104.536	0.345
2452584.630191	104.355	0.316
2452584.674641	104.514	0.324
2452586.639595	104.872	0.278
2452586.684487	104.722	0.907
2452607.617861	104.120	0.253
2452607.571902	104.322	0.303
2452608.601247	103.638	0.244
2452608.557655	104.046	0.142
2452609.536427	104.284	0.384
2452609.581567	103.868	0.581
2452615.544251	104.413	0.401
2452615.587581	104.202	0.434
2452616.537721	104.621	0.377
2452616.581430	104.581	0.376
2452632.539782	104.330	0.574
2452633.540846	104.363	0.669
2452634.541717	104.735	0.313
2452635.543508	104.367	0.404
2452826.830219	105.199	0.536
2452826.874671	105.211	0.269
2452853.759219	105.123	0.292
2452858.869418	104.831	0.364
2452859.880800	104.476	0.351
2452882.681706	104.541	0.204
2454373.642892	104.329	0.116
2454705.631179	104.873	0.065
2454780.500993	105.409	0.292
2454819.320354	105.561	0.084
2455175.419215	105.010	0.063
2455415.686599	104.941	0.061
2455439.606743	105.124	0.060
2455796.671082	105.434	0.077
2455858.545060	105.060	0.060
2456191.589163	105.050	0.045
2456530.687786	104.829	0.054
2456956.535485	104.471	0.094

et al. (2003); 2: Sneden et al. (1996); 3: Cowley & Corliss (1983); 4: Biemont et al. (1981); 5: Biemont et al. (1984); 6: Hannaford et al. (1985); 7: Whaling & Brault (1988); 8: Salih & Lawler (1985); 9: Kwiatkowski et al. (1982); 10: Duquette & Lawler (1985); 11: Corliss & Bozman (1962); 12: Migdalek (1978); 13: Miles & Wiese (1969); 14: McWilliam (1998); 15: Lawler et al. (2001a) 16: DREAM database (Palmeri et al. 2000); 17: Ivarsson et al. (2001); 18: Den Hartog et al. (2003); 19: Lawler et al. (2006); 20: Lawler et al. (2001c); 21: Lawler et al. (2001b); 22: Lawler et al. (2004); 23: Lawler et al. (2008); 24: Lawler et al. (2007); 25: Ivarsson et al. (2003); 26: Grevesse (1969); 27: Nilsson et al. (2002b); 28: Nilsson et al. (2002a). References for hyperfine splitting parameters used are given in column 6, as follows: 1: McWilliam (1998); 2: Lawler et al. (2001a); 3: Ivarsson et al. (2001); 4: Lawler et al. (2001c); 5: Lawler et al. (2001b); 6: Lawler et al. (2004); 7: Mårtensson-Pendrill et al. (1994).

**Table B.1.** Neutron-capture elements linelist and individual abundances in CS 29497-004.

Species	$\lambda(\text{\AA})$	E.P.(eV)	log gf	Ref <sub>log gf</sub> <sup>2</sup>	Ref <sub>HFS</sub> <sup>3</sup>	E.W.(mÅ)	log $\epsilon$
Sr II	3464.45	3.04	0.530	1		syn	0.67
Sr II	4077.71	0.00	0.170	2		syn	0.67
Sr II	4161.79	2.94	-0.600	2		syn(5.4)	0.87
Sr II	4215.52	0.00	-0.170	2		syn	0.77
Y II	3242.28	0.18	0.210	1		65.9	-0.08
Y II	3327.88	0.41	0.130	1		56.3	-0.09
Y II	3549.01	0.13	-0.280	1		52.8	-0.17
Y II	3600.74	0.18	0.280	1		71.6	-0.12
Y II	3611.04	0.13	0.110	1		63.6	-0.27
Y II	3747.56	0.10	-0.910	1		38.7	-0.01
Y II	3774.33	0.13	0.210	1		75.8	-0.13
Y II	3788.69	0.10	-0.070	1		73.6	0.04
Y II	3818.34	0.13	-0.980	1		41.8	0.14
Y II	3832.90	0.18	-0.340	1		56.0	-0.11
Y II	3950.35	0.10	-0.490	1		63.9	0.12
Y II	4398.01	0.13	-1.000	1		39.3	0.01
Y II	4883.68	1.08	0.070	2		35.0	-0.10
Zr II	3334.61	0.56	-0.797	1		30.6	0.78
Zr II	3338.41	0.96	-0.578	1		11.3	0.42
Zr II	3410.24	0.41	-0.323	1		59.8	0.91
Zr II	3424.81	0.04	-1.305	1		27.2	0.59
Zr II	3430.51	0.47	-0.164	1		48.1	0.46
Zr II	3438.23	0.09	0.310	3		88.9	0.86
Zr II	3457.55	0.56	-0.530	1		39.7	0.71
Zr II	3458.92	0.96	-0.520	1		13.0	0.42
Zr II	3479.03	0.53	-0.690	1		26.3	0.50
Zr II	3479.38	0.71	0.170	1		51.4	0.48
Zr II	3499.56	0.41	-0.810	1		22.5	0.38
Zr II	3505.68	0.16	-0.360	1		59.2	0.61
Zr II	3536.93	0.36	-1.306	1		13.3	0.52
Zr II	3551.94	0.09	-0.310	1		65.5	0.67
Zr II	3573.05	0.32	-1.041	1		30.7	0.71
Zr II	3578.21	1.21	-0.607	1		9.4	0.61
Zr II	3630.00	0.36	-1.110	1		25.6	0.69
Zr II	3698.15	1.01	0.094	1		42.2	0.56
Zr II	3714.79	0.53	-0.930	1		34.2	0.85
Zr II	3751.61	0.97	0.012	1		40.1	0.54
Zr II	3766.80	0.41	-0.812	1		40.4	0.73
Zr II	3836.76	0.56	-0.060	4		56.1	0.50
Zr II	3998.95	0.56	-0.387	3		47.1	0.58
Zr II	4050.32	0.71	-1.000	1		17.0	0.64
Zr II	4090.53	0.76	-1.009	1		16.1	0.67
Zr II	4161.21	0.71	-0.720	1		36.3	0.82
Zr II	4208.98	0.71	-0.460	1		38.7	0.61
Nb II	3215.59	0.44	-0.190	6		syn(21.0)	-0.33
Mo I	3864.10	1.00	-0.010	7		syn	0.15
Ru I	3436.74	0.15	0.015	1		syn(11.7)	0.64
Ru I	3498.94	0.00	0.310	8		syn(25.6)	0.62
Ru I	3728.03	0.00	0.270	5		syn	0.55
Ru I	3798.90	0.15	-0.040	5		syn(10.6)	0.56
Ru I	3799.35	0.00	0.020	5		syn(19.5)	0.66
Rh I	3434.89	0.00	0.450	9		syn(11.3)	-0.27
Rh I	3692.36	0.00	0.174	10		syn(12.3)	-0.10
Pd I	3242.70	0.81	-0.070	5		syn	0.31
Pd I	3404.58	0.81	0.320	5		syn(23.6)	-0.07
Pd I	3460.74	0.81	-0.420	5		syn	0.11
Pd I	3516.94	0.96	-0.240	5		syn(10.4)	0.18
Pd I	3634.69	0.81	0.090	11		36.2	0.44
Ag I	3280.68	0.00	-0.050	12		syn(32.5)	-0.58
Ag I	3382.89	0.00	-0.377	12		syn(19.2)	-0.38

Table B.1. continued.

Species	$\lambda(\text{\AA})$	E.P.(eV)	log gf	Ref <sub>log gf</sub>	Ref <sub>HFS</sub>	E.W.(m $\text{\AA}$ )	log $\epsilon$
Ba II	3891.78	2.51	0.280	13		syn	0.22
Ba II	4130.65	2.72	0.560	14	1	syn	0.32
Ba II	4166.00	2.72	-0.420	13		syn	0.52
Ba II	4554.03	0.00	0.170	14	1	syn	0.52
Ba II	4934.08	0.00	-0.150	14	1	syn(166.1)	0.60
La II	3713.54	0.17	-0.800	15	2	syn(12.2)	-0.48
La II	3794.77	0.24	0.210	15	2	syn(45.5)	-0.53
La II	3849.01	0.00	-0.450	15	2	syn(32.4)	-0.47
La II	3949.10	0.40	0.490	15	2	syn	-0.54
La II	3988.51	0.40	0.080	15	2	syn	-0.44
La II	3995.75	0.17	-0.060	15	2	syn	-0.44
La II	4086.71	0.00	-0.070	15	2	syn(52.7)	-0.33
La II	4123.22	0.32	0.130	15	2	syn(47.7)	-0.44
La II	4322.50	0.17	-0.930	15	2	syn(15.2)	-0.32
La II	4333.75	0.17	-0.060	15	2	syn	-0.34
La II	4526.11	0.77	-0.590	15	2	5.9	-0.46
La II	4920.98	0.13	-3.375	15	2	syn(31.3)	-0.13
La II	4921.77	0.24	-1.139	15	2	syn(30.9)	-0.08
Ce II	3539.08	0.32	-0.380	16		8.5	-0.10
Ce II	3577.46	0.47	0.210	16		14.2	-0.26
Ce II	3655.84	0.32	-0.020	16		14.6	-0.23
Ce II	3940.33	0.32	-0.270	16		7.9	-0.33
Ce II	3942.15	0.00	-0.220	16		26.6	-0.09
Ce II	3942.74	0.86	0.730	16		17.8	-0.30
Ce II	3960.91	0.32	-0.400	16		10.6	-0.06
Ce II	3964.50	0.32	-0.540	16		syn	-0.17
Ce II	3984.67	0.96	0.110	16		7.9	0.01
Ce II	3992.38	0.45	-0.170	16		9.1	-0.23
Ce II	3999.24	0.09	0.232	16		24.1	-0.51
Ce II	4003.77	0.93	0.300	16		10.5	-0.07
Ce II	4014.90	0.53	0.140	16		8.5	-0.48
Ce II	4031.33	0.32	-0.080	16		12.9	-0.29
Ce II	4053.50	0.00	-0.710	16		13.4	-0.01
Ce II	4073.47	0.48	0.230	16		20.3	-0.18
Ce II	4083.22	0.70	0.270	16		14.1	-0.16
Ce II	4115.37	0.92	0.100	16		5.9	-0.17
Ce II	4118.14	0.70	0.019	16		11.6	-0.02
Ce II	4120.83	0.32	-0.210	16		11.6	-0.23
Ce II	4127.36	0.68	0.350	16		15.0	-0.24
Ce II	4137.65	0.52	0.440	16		26.0	-0.20
Ce II	4145.00	0.70	0.130	16		8.0	-0.32
Ce II	4165.60	0.91	0.530	16		14.7	-0.17
Ce II	4222.60	0.12	0.020	16		24.2	-0.29
Ce II	4418.78	0.86	0.280	16		10.8	-0.16
Ce II	4486.91	0.30	-0.260	16		17.6	-0.02
Ce II	4539.74	0.33	-0.020	16		17.8	-0.23
Ce II	4562.36	0.48	0.230	16		25.0	-0.11
Ce II	4572.28	0.68	-0.290	16		16.4	0.41
Ce II	4593.93	0.70	0.110	16		13.3	-0.09
Ce II	4628.16	0.52	0.200	16		22.7	-0.10
Pr II	3964.81	0.05	0.121	17	3	syn	-0.72
Pr II	3965.25	0.20	0.135	17	3	syn	-0.62
Pr II	4179.32	0.20	0.480	17	3	syn	-0.65
Pr II	4189.49	0.37	0.380	17	3	syn	-0.67
Pr II	4222.95	0.05	0.270	17	3	syn	-0.65
Pr II	4408.81	0.00	0.180	17	3	syn	-0.72
Nd II	3780.38	0.47	-0.350	18		12.1	-0.06
Nd II	3784.24	0.38	0.150	18		31.7	-0.09
Nd II	3784.84	0.06	-1.040	18		8.0	-0.04
Nd II	3826.41	0.06	-0.410	18		23.3	-0.11
Nd II	3838.98	0.00	-0.240	18		34.6	-0.08

Table B.1. continued.

Species	$\lambda(\text{\AA})$	E.P.(eV)	log gf	Ref <sub>log gf</sub>	Ref <sub>HFS</sub>	E.W.(mÅ)	log $\epsilon$
Nd II	3900.22	0.47	0.100	18		22.8	-0.17
Nd II	3973.26	0.63	0.360	18		25.2	-0.20
Nd II	3990.10	0.47	0.130	18		33.2	0.04
Nd II	4004.01	0.06	-0.736	18		23.3	0.19
Nd II	4013.22	0.18	-1.100	18		4.5	-0.14
Nd II	4018.82	0.06	-0.850	18		13.6	0.00
Nd II	4021.33	0.32	-0.100	18		26.7	-0.06
Nd II	4022.98	0.20	-1.400	18		24.9	1.06
Nd II	4041.06	0.47	-0.530	18		8.6	-0.08
Nd II	4043.59	0.32	-0.710	18		7.4	-0.14
Nd II	4051.14	0.38	-0.300	18		20.1	0.03
Nd II	4059.95	0.20	-0.520	18		18.1	-0.01
Nd II	4061.08	0.47	0.550	18		53.1	0.06
Nd II	4069.26	0.06	-0.570	18		24.3	0.04
Nd II	4109.45	0.32	0.350	18		60.7	0.27
Nd II	4133.35	0.32	-0.490	18		14.3	-0.05
Nd II	4211.29	0.20	-0.860	18		10.0	-0.00
Nd II	4214.60	0.18	-1.180	18		4.2	-0.12
Nd II	4232.37	0.06	-0.470	18		25.6	-0.05
Nd II	4358.16	0.32	-0.160	18		30.9	0.05
Nd II	4446.38	0.20	-0.350	18		26.6	-0.00
Nd II	4462.98	0.56	0.040	18		28.2	0.05
Nd II	4542.60	0.74	-0.280	18		9.3	-0.04
Nd II	4567.60	0.20	-1.250	18		2.9	-0.23
Nd II	4579.31	0.74	-0.480	18		7.2	0.04
Nd II	4597.01	0.20	-1.150	18		8.1	0.14
Nd II	4645.76	0.56	-0.760	18		7.9	0.14
Nd II	4706.54	0.00	-0.710	18		23.7	0.02
Nd II	4715.59	0.20	-0.900	18		9.5	-0.04
Nd II	4859.03	0.32	-0.440	18		20.1	0.01
Sm II	3706.75	0.49	-0.600	19		8.2	-0.24
Sm II	3760.71	0.19	-0.400	19		23.7	-0.23
Sm II	3793.98	0.10	-0.670	19		15.9	-0.29
Sm II	3896.97	0.04	-0.670	19		15.5	-0.39
Sm II	3993.31	0.04	-0.930	19		13.7	-0.21
Sm II	4023.22	0.04	-0.930	19		11.3	-0.31
Sm II	4206.12	0.38	-0.720	19		6.8	-0.40
Sm II	4318.93	0.28	-0.250	19		23.0	-0.36
Sm II	4420.52	0.33	-0.430	19		30.2	0.043
Sm II	4499.48	0.25	-0.870	19		9.9	-0.25
Sm II	4519.63	0.54	-0.350	19		12.0	-0.34
Sm II	4523.91	0.43	-0.390	19		14.0	-0.34
Sm II	4537.94	0.48	-0.480	19		10.6	-0.34
Sm II	4577.69	0.25	-0.650	19		13.7	-0.31
Sm II	4591.81	0.19	-1.120	19		5.1	-0.40
Sm II	4642.23	0.38	-0.460	19		16.8	-0.25
Sm II	4815.81	0.19	-0.820	19		9.6	-0.42
Eu II	3724.93	0.00	-0.090	20	4	syn(98.6)	-0.65
Eu II	3819.67	0.00	0.510	20	4	syn	-0.65
Eu II	3907.11	0.21	0.170	20	4	syn(75.7)	-0.65:
Eu II	3930.50	0.21	0.270	20	4	syn(91.1)	-0.68
Eu II	3971.97	0.21	0.270	20	4	syn	-0.77
Eu II	4129.73	0.00	0.220	20	4	syn(133.6)	-0.65
Eu II	4205.04	0.00	0.210	20	4	syn	-0.65
Eu II	4435.58	0.21	-0.110	20	4	0.0	0.00
Eu II	4522.58	0.21	-0.670	20	4	0.0	0.00
Gd II	3331.39	0.00	-0.140	1		25.9	-0.37
Gd II	3424.59	0.35	-0.170	1		11.6	-0.42
Gd II	3439.21	0.38	0.150	1		26.5	-0.23
Gd II	3451.24	0.38	-0.050	1		11.5	-0.52
Gd II	3454.91	0.03	-0.480	1		16.1	-0.31



Table B.1. continued.

Species	$\lambda(\text{\AA})$	E.P.(eV)	log gf	Ref <sub>log gf</sub>	Ref <sub>HFS</sub>	E.W.(mÅ)	log $\epsilon$
Gd II	3481.80	0.49	0.230	1		19.6	-0.38
Gd II	3549.36	0.24	0.260	1		30.0	-0.43
Gd II	3557.06	0.60	0.210	1		15.1	-0.40
Gd II	3697.73	0.03	-0.280	1		syn	-0.24
Gd II	3712.70	0.38	0.150	1		syn	-0.29
Gd II	3768.40	0.08	0.360	1		47.8	-0.37
Gd II	3796.38	0.03	0.140	1		49.4	-0.17
Gd II	3844.58	0.14	-0.400	1		23.4	-0.14
Gd II	3916.51	0.60	0.060	2		16.3	-0.29
Gd II	3973.98	0.60	-0.400	1		4.7	-0.45
Gd II	4037.32	0.66	-0.020	1		16.3	-0.16
Gd II	4037.89	0.56	-0.230	1		7.4	-0.46
Gd II	4085.56	0.73	0.070	1		9.3	-0.46
Gd II	4191.07	0.43	-0.570	1		10.0	-0.15
Gd II	4215.02	0.43	-0.580	1		10.6	-0.11
Tb II	3472.80	0.13	-0.100	21	5	0.0	0.00
Tb II	3568.45	0.00	0.360	21	5	syn	-1.06
Tb II	3600.38	0.64	0.600	21	5	syn	-1.14
Tb II	3658.89	0.13	-0.010	21	5	syn(7.5)	-1.01
Tb II	3702.85	0.13	0.440	21	5	syn(25.6)	-1.04
Tb II	3848.73	0.00	0.280	21	5	syn	-1.04
Tb II	3874.17	0.00	0.270	21	5	syn	-0.96
Tb II	3899.19	0.37	0.330	21	5	syn	-1.04
Tb II	4002.57	0.64	0.100	21	5	syn	-1.01
Tb II	4005.47	0.13	-0.020	21	5	syn(12.3)	-1.11
Dy II	3407.80	0.00	0.180	1		56.0	-0.06
Dy II	3434.37	0.00	-0.450	1		32.8	-0.10
Dy II	3445.57	0.00	-0.150	1		44.9	-0.08
Dy II	3454.32	0.10	-0.140	1		36.7	-0.20
Dy II	3460.97	0.00	-0.070	1		46.8	-0.12
Dy II	3536.02	0.54	0.530	1		46.0	-0.14
Dy II	3538.52	0.00	-0.020	1		54.7	0.05
Dy II	3546.83	0.10	-0.550	1		26.5	-0.06
Dy II	3550.22	0.59	0.270	1		30.3	-0.22
Dy II	3559.30	1.22	-0.280	1		3.5	-0.11
Dy II	3563.15	0.10	-0.360	1		34.4	-0.06
Dy II	3694.81	0.10	-0.110	1		47.2	-0.06
Dy II	3708.22	0.59	-0.880	1		5.9	-0.04
Dy II	3747.82	0.10	-0.810	1		15.9	-0.18
Dy II	3788.44	0.10	-0.570	1		29.4	-0.05
Dy II	3869.86	0.00	-0.940	2		17.4	-0.14
Dy II	3983.65	0.54	-0.310	1		21.6	-0.04
Dy II	3996.69	0.59	-0.260	1		19.3	-0.10
Dy II	4073.12	0.54	-0.320	1		23.2	0.00
Dy II	4077.97	0.10	-0.040	1		63.8	0.22
Dy II	4103.31	0.10	-0.380	1		44.5	0.05
Dy II	4468.14	0.10	-1.670	1		4.5	-0.03
Ho II	3796.75	0.00	0.160	22	6	syn	-0.78
Ho II	3810.74	0.00	0.190	22	6	syn	-0.77
Ho II	4045.47	0.00	-0.050	22	6	syn	-0.70
Ho II	4152.59	0.08	-0.930	22	6	0.0	0.00
Er II	3332.70	0.89	0.070	23		11.0	-0.37
Er II	3499.10	0.05	0.290	23		48.0	-0.49
Er II	3559.89	0.00	-0.690	23		22.6	-0.25
Er II	3692.65	0.05	0.280	23		59.2	-0.28
Er II	3729.52	0.00	-0.590	23		28.4	-0.27
Er II	3786.84	0.00	-0.520	23		35.1	-0.19
Er II	3830.48	0.00	-0.220	23		45.1	-0.26
Er II	3896.23	0.05	-0.120	23		53.4	-0.11
Er II	3938.63	0.00	-0.520	23		27.5	-0.39
Tm II	3462.20	0.00	0.030	1		syn(24.0)	-1.24

Table B.1. continued.

Species	$\lambda(\text{\AA})$	E.P.(eV)	log gf	Ref <sub>log gf</sub>	Ref <sub>HFS</sub>	E.W.(mÅ)	log $\epsilon$
Tm II	3700.26	0.03	-0.290	1		syn(16.7)	-1.18
Tm II	3701.36	0.00	-0.540	1		syn(10.8)	-1.20
Tm II	3761.33	0.00	-0.430	1		syn	-1.25
Tm II	3795.76	0.03	-0.230	1		syn(16.3)	-1.15
Tm II	3848.02	0.00	-0.130	1		syn(27.1)	-1.10
Yb II	3289.37	0.00	0.020	1	7	syn	-0.20
Yb II	3694.19	0.00	-0.300	1	7	syn	-0.30
Lu II	3397.02	1.46	-0.190	1	1	syn	-0.72
Lu II	3472.45	1.54	-0.190	1	1	syn	-1.02:
Lu II	3554.39	2.15	0.140	1	1	syn	-1.02
Hf II	3389.829	0.45	-0.780	24		syn	-0.75
Hf II	3399.793	0.00	-0.570	24		syn(34.6)	-0.62
Hf II	3479.289	0.38	-1.000	24		syn	-0.60
Hf II	3505.219	1.04	-0.140	24		syn	-0.75
Hf II	3561.659	0.00	-0.870	24		syn	-0.80
Hf II	3719.276	0.61	-0.810	24		syn	-0.65
Hf II	3793.379	0.38	-1.110	24		syn	-0.50
Hf II	3918.094	0.45	-1.140	24		syn	-0.60
Hf II	4093.155	0.45	-1.150	24		syn	-0.65
Os I	3267.95	0.00	-1.080	25		syn(13.0)	0.36
Os I	3301.57	0.00	-0.743	25		syn	0.27
Os I	3528.60	0.00	-1.740	25		syn(7.5)	0.47
Os I	4135.77	0.52	-1.260	25		syn(6.2)	0.62
Os I	4260.85	0.00	-1.440	25		syn(8.2)	0.37
Ir I	3513.65	0.00	-1.246	25		syn(25.7)	0.25
Ir I	3800.12	0.00	-1.489	25		syn(15.2)	0.22
Pt I	3301.86	0.81	-0.770	1		syn	0.10:
Pt I	3315.04	0.00	-2.580	1		syn	0.78:
Pb I	4057.81	1.32	-0.220	26		syn	0.05:
Th II	3351.23	0.19	-0.600	27		syn(10.7)	-0.90
Th II	3435.98	0.00	-0.670	27		syn(4.7)	-1.05
Th II	3469.92	0.51	-0.129	27		syn	-1.05
Th II	3675.57	0.19	-0.840	27		syn(2.2)	-1.00
Th II	4019.13	0.00	-0.228	27		syn(16.0)	-1.25
Th II	4086.52	0.00	-0.929	27		syn	-1.15
U II	3859.57	0.04	-0.067	28		syn	-2.20: